

A panoramic VISTA of the stellar halo of NGC 253 [★]

L. Greggio¹, M. Rejkuba^{2,3}, O. A. Gonzalez⁴, M. Arnaboldi², E. Iodice⁵, M. Irwin⁶, M.J. Neeser², and J. Emerson⁷

¹ INAF, Osservatorio Astronomico di Padova, Vicolo dell'Osservatorio 5, 35122 Padova, Italy
e-mail: greggio@pd.astro.it

² ESO, Karl-Schwarzschild-Strasse 2, D-85748 Garching, Germany
e-mail: [mrejckuba], [marnabol], [mneeser]@eso.org

³ Excellence Cluster Universe, Boltzmannstr. 2, D-85748, Garching, Germany

⁴ ESO, Ave. Alonso de Cordova 3107, Casilla 19, Santiago 19001, Chile
e-mail: ogonzale@eso.org

⁵ INAF, Osservatorio Astronomico di Capodimonte, 80126, Napoli, Italy

⁶ Institute of Astronomy, Madingley Road, Cambridge CB03 0HA, UK

⁷ Astronomy Unit, School of Physics and Astronomy, Queen Mary University of London, Mile End Road, London, E1 4NS, UK

Draft date 12.09.2013; Received date; accepted date

ABSTRACT

Context. Outskirts of large galaxies contain important information about galaxy formation and assembly. Resolved star count studies can probe the extremely low surface brightness of the outer halos.

Aims. NGC 253 is a nearly edge-on disk galaxy in the Sculptor group where we resolved the halo stars from ground-based images, with the aim of studying its stellar population content, the structure and the overall extent of the halo.

Methods. We use Z and J-band images from the VIRCAM camera mounted on the VISTA telescope to construct the spatially resolved J vs. Z-J colour-magnitude diagrams (CMDs). The very deep photometry and the wide area covered allows us to trace the red giant branch (RGB) and asymptotic giant branch (AGB) stars that belong to the halo of NGC 253 out to 50 kpc along the galaxy minor axis.

Results. We confirm the existence of an extra planar stellar component of the disk, with a very prominent southern shelf and a symmetrical feature on the north side. The only additional visible sub-structure is an overdensity in the north-west part of the halo ~ 28 kpc distant from the plane and extending over 20 kpc parallel with the disk. We measure the transition from the disk to the halo at a radial distance of about 25 kpc with a clear break in the number density profile. The isodensity contours show that the inner halo is a flattened structure that blends with a more extended, diffuse, rounder outer halo. Such external structure can be traced to the very edge of our image out to 50 kpc from the disk plane. The number density profile of the stars in the stellar halo follows a power law with index -1.6 , as function of radius. The CMD shows a very homogeneous stellar population across the field; by comparing with isochrones we conclude that the RGB stars are ~ 8 Gyr old or more, while the AGB stars trace a population of about $2 \times 10^8 M_{\odot}$ formed from ~ 0.5 to a few Gyr ago. Surprisingly, part of this latter population appears scattered over a wide area. We explore several ideas to explain the origin of this relatively young component in the inner halo of NGC 253.

Key words. Galaxies: spiral – Galaxies: Individual: NGC 253 – Galaxies: star clusters

1. Introduction

The impressive evidence of stellar streams in the outer regions of galaxies (e.g. Ferguson et al. 2002; Martínez-Delgado et al. 2008, 2009, 2010; Mouhcine et al. 2010; Chonis et al. 2011; Miskolczi et al. 2011) dramatically shows the importance of merging in their formation, and at the same time discloses how the study of the stellar populations in the halos of galaxies can be effective for understanding the galaxy formation process. Indeed, although the halo contains only a small fraction of the mass of the galaxy, the long dynamical times keep the memory of the assembly history of the galaxy over a considerable fraction of its life. It is then of great interest to probe the extent of the halo, its structure and amount of substructure, and its stellar population content.

The panoramic view of the M31 - M33 complex (McConnachie et al. 2009) has revealed the presence of sev-

eral substructures, scattered over the whole probed volume, that are remnants of interactions of M31 with its less massive neighbours. A similar situation likely holds for the Milky Way, as indicated by the presence of the Sagittarius Dwarf (Ibata et al. 1994), and other structures (e.g. Yanny et al. 2003; Ibata et al. 2003; Belokurov et al. 2006; Jurić et al. 2008; Grillmair 2009, and references therein). For both the Milky Way and the Andromeda galaxy, these substructures seem to reside above a diffuse halo, which can hardly have originated from the late disruption of dwarfs, due to the very long dynamical timescale in such low density regions of galaxies. The presence of this underlying halo is particularly puzzling in the frame of the current picture of galaxy formation in a Cold Dark Matter universe, and substantial effort is invested to hunt for this elusive component in nearby galaxies (Rejkuba et al. 2009; Jablonka et al. 2010; Tanaka et al. 2011; Barker et al. 2012; Cockcroft et al. 2013; Monachesi et al. 2013).

The amount of substructure in the halo traces its buildup through hierarchical accretion and merger episodes. In the Milky Way, Bell et al. (2008) measured 30-40% RMS fluctuation in

Send offprint requests to: L. Greggio

[★] Based on observations taken within the VISTA Science Verification Program ID 60.A-9285(A)

the stellar distribution of the halo stars with respect to a smooth model, while Starkenburg et al. (2009) estimated a minimum fraction of accreted stars in the halo of 10%. Evidence of incompletely mixed sub-populations was also found in the inner halo of NGC 891, where the RMS fluctuation in stellar distribution is 14% (Ibata et al. 2009). An additional feature which is gaining reliability in the literature is that the stellar halo may actually consist of two components, one more internal, elongated, and relatively metal rich, and one external, almost spherical and metal poor (Carollo et al. 2007).

On the theoretical side, sophisticated galaxy formation models in a Λ CDM universe have been developed, with specific predictions about the stellar population properties and surface brightness profiles which can be compared to observations (Abadi et al. 2006; Zolotov et al. 2009; Cooper et al. 2010; Font et al. 2011).

An analysis of the simulated stellar halos of Cooper et al. (2010), that were formed via satellite galaxy accretions within the cosmological N-body simulations of the Aquarius project, showed a systematically larger RMS in the stellar density distribution with respect to the one measured for the Milky Way halo by Bell et al. (2008) on the Sloan Digital Sky Survey data. Based on that Helmi et al. (2011) estimated that $\sim 10\%$ of the Milky Way halo stars formed *in situ*. According to Font et al. (2011) simulations, who instead used the GIMIC suite of cosmological hydrodynamical simulations, the inner halo stars are predominantly formed *in situ*, while the outer regions of the halo should be mostly populated with stars originating from accreted satellites. The *in situ* component in these simulations comes from a proto-disk formed at high redshift, which later had its stars dispersed to form the inner halo via dynamical heating associated with mass accretion (McCarthy et al. 2012). As a consequence, these models are characterized by a change of slope of the surface brightness increase with radius, which occurs at about 30 kpc for a Milky Way type of galaxy. The different proportions of *in situ* star formation would also account for a general metallicity gradient with high metallicity stars found preferentially in the inner regions.

Studying the stellar distribution in the outskirts of galaxies has great potential to constrain these models. To this end, the best suited objects are (massive) spiral galaxies viewed edge on, because of the favorable geometry to trace the stellar halo. NGC 253 is one such galaxy. It is sufficiently near to allow us to map its oldest stellar population, traced by bright Red Giant Branch (RGB) stars. The wide field of view of the VISTA telescope offers the opportunity to study the stellar content in the outskirts of its disk and in its halo in one shot. Notice that the extended halo is characterized by very low surface brightness, down to $\mu_V \approx 33$ mag/square arcsec or fainter. Reaching these levels (many magnitudes fainter than the sky) with surface photometry is extremely challenging (Zackrisson et al. 2012), while photometry of individual stars has proved very successful (e.g. Ibata et al. 2007).

In these kinds of studies foreground and background contamination is an important issue, due to the intrinsically low surface density of the sought after stellar halo. In this respect, NGC 253 is favourably located at high Galactic latitude ($b = -88^\circ$), such that the foreground extinction is very low ($E(B - V) = 0.02$) and we expect the foreground sources to be fairly uniformly distributed in the VISTA field of view. This is an advantage with respect to studying the halos of large Local Group galaxies, where the wide solid angle is more likely to intercept local structures and foreground inhomogeneities.

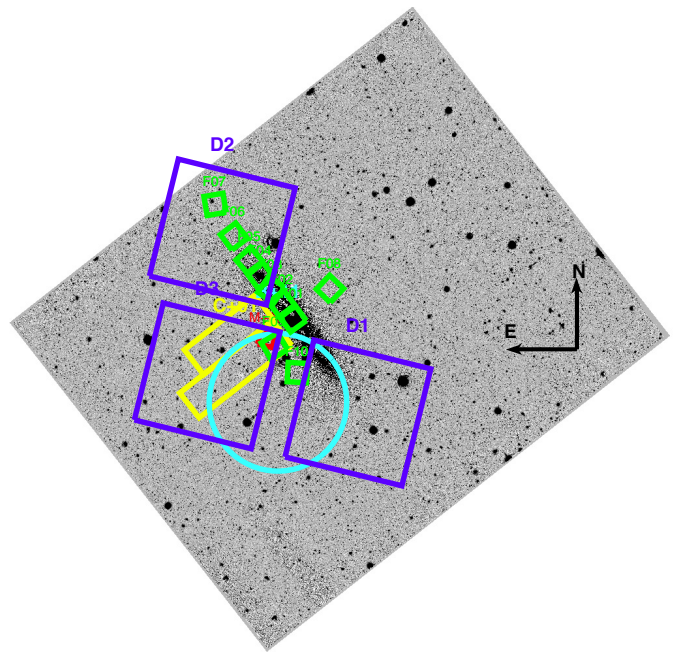


Fig. 1. VISTA image of NGC 253 with over plotted the field of view of previous resolved stellar population studies from the literature; specifically IMACS@Magellan (Bailin et al. 2011, cyan circle), 3 WIRCam@CFHT fields (Davidge 2010, large blue squares), NTT SUSI2 (Comerón et al. 2001, yellow rectangles), and many ACS fields (GHOST survey, Radburn-Smith et al. 2011, small green squares). The HST WFC2 field from Mouhcine et al. (2005a, small red square) partially overlaps with ACS, SUSI2, and IMACS fields. The wide coverage of the VISTA data can be readily appreciated.

NGC 253 is the brightest ($M_B \sim -20$) member of the Sculptor group, which is an extended filament of galaxies with distances ranging from ~ 2 to 4.5 Mpc (Jerjen et al. 1998; Karachentsev et al. 2003). NGC 253 is a luminous infrared source which hosts a recent starburst in its central part and sustains a galactic wind (Rieke et al. 1980, 1988). Its inner regions and X-ray properties were studied by many authors (e.g. Fabbiano & Trinchieri 1984; Westmoquette et al. 2011, and references therein). The strong nuclear outflow in NGC 253 is traced by huge lobes of diffuse X-ray, UV, $H\alpha$, HI, and far-IR dust emission that extend up to ~ 9 kpc away from the disk (Strickland et al. 2002; Bauer et al. 2008; Hoopes et al. 2005; Boomsma et al. 2005; Kaneda et al. 2009).

This outflow is driven by widespread star formation activity, which is not only confined to the nuclear starburst but is also evidenced by bubble like structures visible on the disk (Sofue et al. 1994), as well as by the young supergiant stars in Colour-Magnitude Diagrams (CMDs) of resolved stars (Dalcanton et al. 2009; Davidge 2010; Radburn-Smith et al. 2011). Comerón et al. (2001) find young stars along the minor axis, up to 15 kpc away from the galaxy plane, suggesting local star formation in the outflow (see also Comerón et al. 2003). This strong activity may be surprising given that there is no close companion, but NGC 253 shows clear signs of interaction, as kinematically distinct structures in the centre of the galaxy (Prada et al. 1998), extra-planar gas and stars, and pronounced asymmetries in the stellar distribution (Davidge 2010). The evidence suggests that this galaxy has experienced a secondary event during its formation.

Pencil beam, deep HST observations of NGC 253 have been made by Mouhcine et al. (2005a,b) with the WFPC2 camera, while the ANGST (Dalcanton et al. 2009) and the GHOSTS teams (Radburn-Smith et al. 2011) observed with the ACS. The location of the tip of the RGB in the ACS data indicates a distance modulus of 27.7, slightly larger but fully consistent with the distance determined by Mouhcine et al. (2005a) from WFPC2 data ($27.59 \pm 0.06 \pm 0.16(\text{sys})$). Some of these HST fields are located in the periphery of the disk, but are close to it, while the outer regions of the galaxy were more extensively probed with wide field imaging from the ground. Malin & Hadley (1997) traced an extended low surface brightness envelope of about 28 mag arcsec⁻² out to 25' (corresponding to ≈ 25 kpc) distance around NGC 253, noticing the asymmetrical nature of this stellar halo, and concluding that it might have been distorted by the infall of a companion galaxy. Deeper imaging that resolved individual stars in the halo were published by Davidge (2010), and Bailin et al. (2011). The former study is not deep enough to sample the RGB stars, so that most of the information concerns the disk and the extra-planar young and intermediate-age component, as traced by young red supergiants and asymptotic giant branch (AGB) stars. This study reveals that the disk of NGC 253 is disturbed. Bailin et al. (2011) are instead able to trace the RGB population in a wide region which comprises the inner halo for which they find a rather flattened geometry. Both studies find a stellar over density in the south, outer disk region, confirming early finding by Beck et al. (1982).

In this paper we present deep Z and J band photometry of the outer disk and halo of NGC 253 obtained with the VISTA telescope in the framework of the Science Verification Programme. In Fig. 1 we provide an overview of the several pointings from the literature, which were used to investigate resolved stellar populations in NGC 253, superimposed on the VISTA image. In comparison to these previous works, our data offer the opportunity to study the whole region around NGC 253, yielding a wide and continuous view of the halo out to a distance of ~ 50 kpc. In Section 2 we describe the data, and in Section 3 present the Colour-Magnitude Diagram (CMD) constructed with the stellar source catalogue. In Section 4 we discuss the stellar disk and the halo components of NGC 253 plus the perturbation to the disk, i.e. the southern shelf, and report about the detection for the first time of a substructure in the halo, at about 30 kpc from the main plane of the disk. In Section 5 we discuss the star formation history in the outer disk and halo of NGC 253, and the spatial distribution of both AGB and RGB population in these two components. Our results are summarized and discussed in Section 6, and conclusions are drawn in Section 7. Throughout this paper we adopt a distance modulus to NGC 253 of 27.7 mag, which is equivalent to a distance of 3.47 Mpc, yielding an image scale of 16.8 pc per arcsecond.

2. The data

The data presented in this paper were collected as part of the VISTA Science Verification (SV) programme (Arnaboldi et al. 2010) which was designed to test the performance of the integrated telescope-instrument system with two projects: (i) one aimed at deriving very deep images in the smallest contiguous area that uses all VISTA's large field of view (a *tile* in VISTA nomenclature) whose results are the subject of this paper; (ii) the other covering a 30 deg² area around Orion Belt stars with a mosaic of 20 tiles having shallower exposures (Petr-Gotzens et al. 2011). The two projects required different observing strategies, therefore providing tests of observing templates and operation

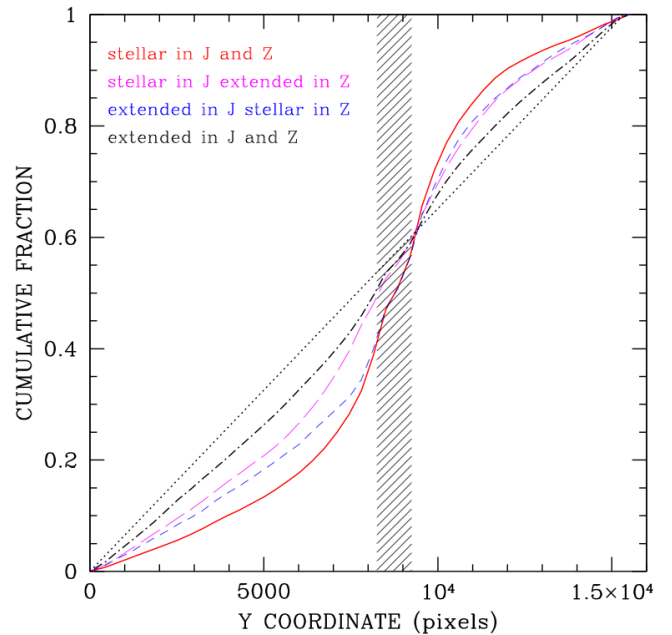


Fig. 2. Cumulative distribution along the vertical coordinate of the VISTA tile for sources with different classifications on the VDFS catalogue: stellar in both *J* and *Z* (red solid line), extended in both *J* and *Z* (black dot-dashed line), stellar in *J* and extended in *Z* (magenta long-dashed line), stellar in *Z* and extended in *J* (blue short-dashed line). A flat spatial distribution corresponds to a line at 45 degrees (dotted line). The shaded region indicates the location of the disk of NGC 253, where the surface brightness is too high to measure individual sources and number counts are heavily affected by crowding effects.

tools for the public surveys which started on the VISTA telescope immediately after the SV (Arnaboldi et al. 2012).

2.1. Observations

During the SV period (from October 16 to November 2, 2009), NGC 253 was observed in the first part of the night, until the second SV target, Orion, became observable.

VISTA is a 4m alt-azimuth telescope with a single instrument: VIRCAM (Emerson et al. 2006; Dalton et al. 2006). The camera has a 1.65 degree diameter field of view which is sparsely populated with 16 2k \times 2k Raytheon VIRGO detectors with pixels of mean size $\sim 0''.34$. Each individual exposure images a (disconnected) total area of 0.59 deg². To sample a contiguous field of $\sim 1.5 \times 1$ deg² at least 6 individual exposures (so called pawprints) are necessary with large offsets. Since in this project we aimed to get deep photometry, the single tile centred on RA=00:46:59.86, DEC=-25:16:31.8 was imaged many times over the two week long observing run. Each observing sequence typically consisted of several (2-5) jittered exposures at one pawprint position, before making a larger offset to the next pawprint position to cover the gap. At this second position the same number of jittered exposures were taken and repeated until six pawprints were accumulated to fill the tile. These sequences were then repeated with different filters.

In spite of the large extent of the target on the sky, (NGC 253 is one of the largest southern galaxies), the observing strategy did not require extra offset empty sky fields due to the very

large size of each VIRCAM detector, which covers an area of $11'6 \times 11'6$ on sky. The galaxy major axis was oriented at $PA = 51.95^\circ$, aligned with the shorter side of the tile, such that the galaxy covered detectors 10 and 11 in pawprints 2, 4, and 6, while it was kept in the gap between the detectors in the other three pawprints. Hence the jittered exposures of the odd pawprints could be used to create sky images for the data processing, while at the same time being used in the final deep stack.

We acquired deep images of NGC 253 in three filters: Z, J and in NB118. The latter is a narrow band filter centred on the redshifted wavelength of $H\alpha$ emitters at redshift $z \sim 0.84$ and $Ly\alpha$ emitters at $z \sim 8.8$ (Milvang-Jensen et al. 2013). While the data taken with that filter were focused on the high redshift universe behind NGC 253, with the deep J and Z-band images we explore the stellar population content and the structure of the halo of NGC 253. The J-band images consisted of 5 exposures, each with a detector integration time (DIT) of 45 sec. The Z-band images had 3×60 sec exposure, while several different DITs were used for NB118 images: 270, 450 and 860 sec. The final deep J-band stack was made combining 20 tile sequences of 6 pawprints with a varying number of jitters that add up to 22.1h total accumulated exposure time. The total exposure time of all Z-band sequences was 9.6h, and 5.8h were accumulated with the NB118 filter. On target exposure time is 1/3 of the total accumulated exposures due to large offsets necessary to fill the gaps between detectors. These integration times allowed us to reach $J=23.5$ and $Z=24.5$ (on the Vega magnitude system) with a S/N of 3.

In addition, we acquired shallower exposures in all the VISTA broad-band filters (Z, Y, J, H and Ks) with the aim of studying the central part of the disk of NGC 253 and its structure. In this paper we analyze the deep Z and J-band images, while the shallow broad-band imaging data are described in a subsequent paper (Iodice et al., in prep).

During the observing run the seeing and sky transparency varied, but the conditions were generally very good, with only two nights having thin clouds (but excellent seeing) and two nights being lost due to strong wind. The final deep stacked image has an average seeing of $\sim 0''.9$ in the J-band and $\sim 1''.2$ in the Z-band.

Figure 1 shows the final stacked J-band image, mapped with $\approx 13000 \times 16000$ pixels. At the distance of NGC 253 the image samples an area of about $74 \text{ kpc} \times 91 \text{ kpc}$ around NGC 253.

2.2. Data Reduction and Photometry

Data reduction was carried out with the VISTA Data Flow System (VDFS, Lewis et al. 2010) at the Cambridge Astronomy Survey Unit (CASU). The reduction procedure consists of the following standard steps: dark correction which removes the dark current and also corrects other additive electronic effects; linearity correction to account for the non-linear overall response of the VISTA detectors; flatfield correction using stacked twilight flats which is also used to gain-normalise all the detectors to a common internal system; and sky background correction to remove the large-scale spatial background variation from atmosphere variations. In addition, the VISTA detector IRACE controllers imprint a low-level horizontal stripe pattern on the images. While the position and amplitude of the stripes varies from one exposure to the next, it is the same along the row across the four detectors read out through each IRACE controller. Therefore, even though the extended and bright galaxy was occupying the whole of detector number 10 and a large fraction of detector 11, the other two detectors could be used to

move the striping pattern from the galaxy images. The pipeline then combines the individual jittered exposures for each OB to make deeper individual pawprint stacks, and the six stacked pawprints are combined to produce a tile image (and catalogue) for each OB.

The final deep stacked tile image and catalogue used for the science analysis was created by first combining all suitable sets of 6 pawprint stacks to make deeper pawprint stacks. Prior to making the final tile image any background variation in the pawprint component images was removed using the so-called nebosity filter developed by CASU¹. This filter differentially removes all smoothly varying background on a specified scale, in this case set to ≈ 30 arcsec. In addition to generic background variations the filter also drastically reduces the impact of large-scale reflection halos around bright stars and also removes most of the unresolved disk/halo light from NGC 253.

These "nebulised" pawprint images were then combined to make the final deep tile image. A few individual OB exposures were affected by electronic noise appearing occasionally on channel 14 of detector 6. However, the total area affected by that extra noise was less than 0.4% of the whole tile, and as most images did not have this extra noise present this was effectively removed during the data reduction. In contrast the upper half of detector 16 (which covers the southern corner of the tile in Fig. 1) is unstable, particularly in the bluer bands, and was masked off in the confidence maps prior to making the final tile images. Although the whole tile image is available, objects falling on this part of detector 16 have shorter effective integration times, by a factor 2, compared to the rest of the tile resulting in shallower photometry in the affected regions. Finally, prior to making the deep Z- and J-band catalogues the central region of NGC253 was masked out. No other masks, e.g. for bright foreground stars, were used.

The cataloguing and photometric measurements were done with the VDFS pipeline using the standard CASU imcore package. This package measures fluxes in a range of apertures and enables shape characterization for all objects. The deblending option was used to enable better measures of stellar sources in the crowded outer disk regions of the galaxy. The shape parameters and series of apertures fluxes were used to generate morphological classification information and to compute stellar aperture corrections. Photometric (and astrometric) calibration was based on unsaturated 2MASS stars converted to the VISTA (Vega-like) system.

The photometric errors as a function of magnitude are well fitted with an exponential function:

$$\sigma_J = 5.58 \times 10^{-10} \times e^{0.803 \times J + 1.17} \quad (1)$$

$$\sigma_Z = 1.87 \times 10^{-9} \times e^{0.774 \times Z - 0.026} \quad (2)$$

The catalogue from the VDFS pipeline includes more than 400,000 sources matched on the J and on the Z tiles, but $\sim 30\%$ of them are either spurious sources, or their magnitude and/or shape are very uncertain. Most of these objects are classified as noise in either band, and a few of them are instead saturated or contain a bad pixel. We do not consider these detections in the following analysis. In addition, for $\sim 10\%$ of the remaining objects, the positional coincidence of the source on the two tiles is particularly poor. We also discard these cases, since we aim at the construction of a catalogue of NGC 253 bona fide star members, and the poor quality of the positional match may indicate the presence of an extended object or a blend of two or more stars. After this cleaning, the catalogue includes about 253,500

¹ see <http://casu.ast.cam.ac.uk/publications/nebulosity-filter>

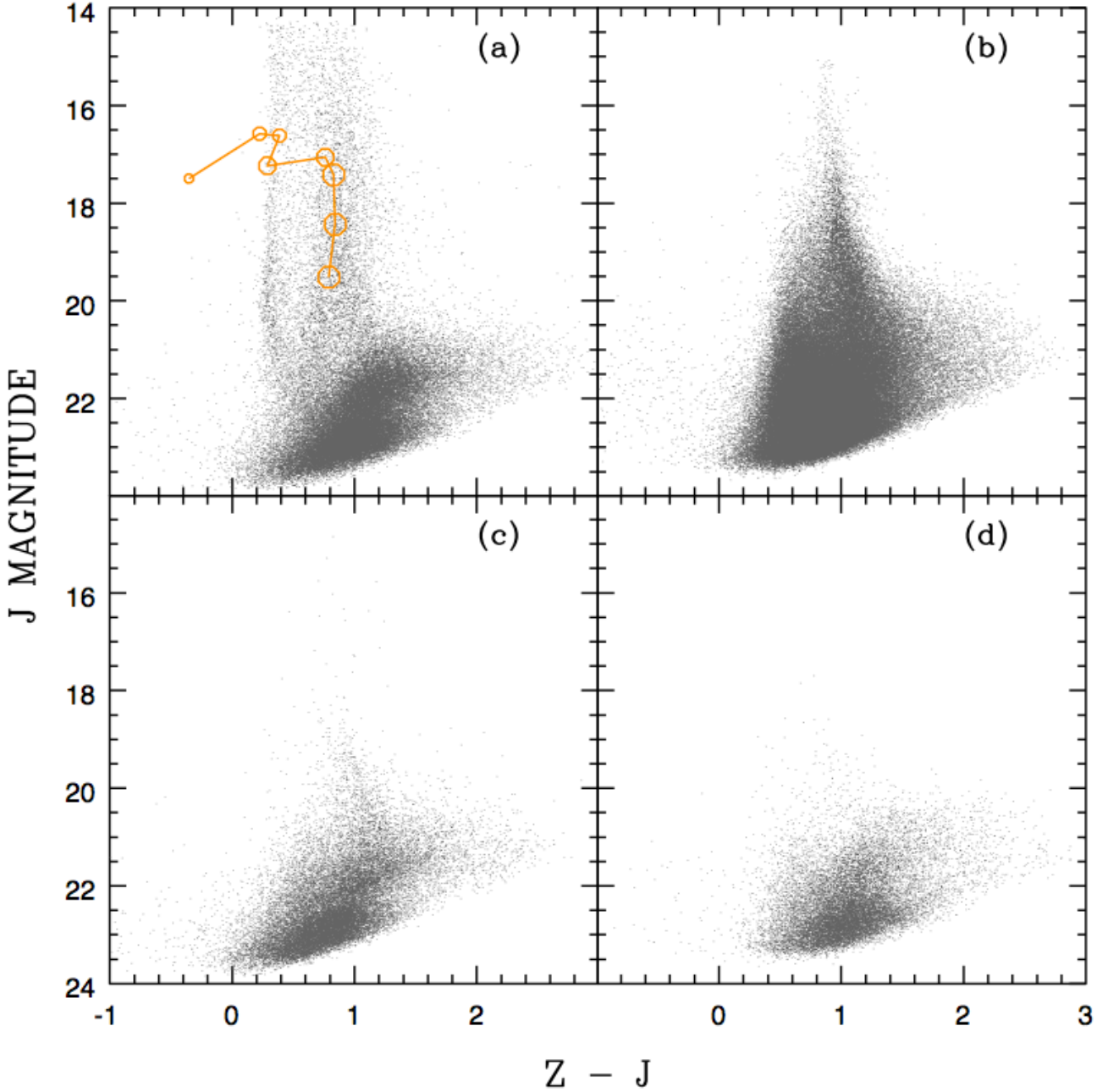


Fig. 3. Observed CMDs for objects with different classifications from the reduction package: stellar sources on both filters (panel (a), 55025 points); extended sources in both filters (panel (b), 151924 points); stellar on the J and extended on the Z tile (panel (c), 27687 points); and extended on the J and stellar on the Z image (panel (d), 18932 points). In panel (a) the open (orange) circles show the evolutionary path of a simple stellar population (SSP) model with metallicity $Z=0.008$ as the population ages. The size of the circles increases with the age of the model plotted at (4, 10, 30, 100 and 300) Myr and at (1, 3 and 10) Gyr. The model was obtained using the CMD on-line tool by L. Girardi at stev.oapd.inaf.it/cmd, and refers to an SSP born with $10^5 M_{\odot}$ of stars distributed between 0.1 and $100 M_{\odot}$ with a Salpeter IMF flattened below $0.5 M_{\odot}$.

sources classified as *stellar* or *extended* in either the J or Z tile, or both. Inspection of the spatial distribution of the various categories of sources shows that all of them are concentrated toward the disk of NGC 253. This is due to crowding, since the de-blending of stellar sources becomes progressively more difficult as the surface brightness increases. This effect enhances the number of sources classified as *extended* as the galaxy disk is approached. However, the spatial distribution of these four

kinds of detections show quantitative differences, as illustrated in Fig. 2. Sources classified as *extended* on both tiles deviate the least from a flat distribution, while sources classified as *stellar* on both tiles deviate the most, with a strong excess in the shaded region, where the disk is located. Sources classified differently on the two tiles exhibit a behavior which is intermediate between the flat distribution and the population concentrated toward the disk of NGC 253.

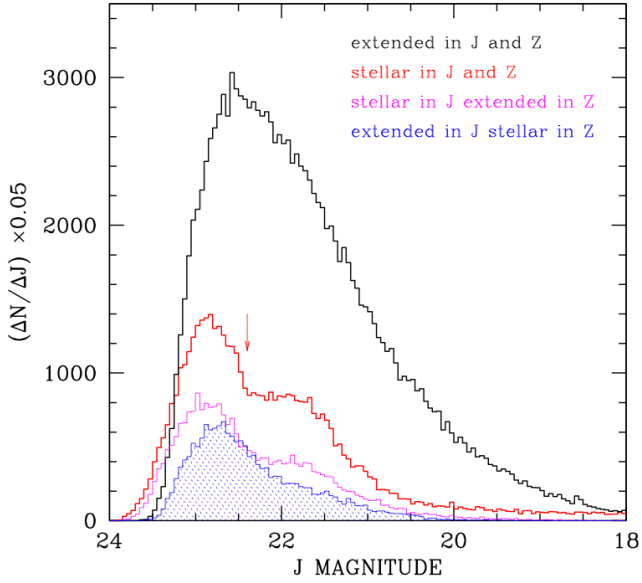


Fig. 4. Luminosity functions of the different kinds of sources whose CMDs are shown in Fig. 3. The red thick line shows the distribution of sources classified as stellar in both filters corresponding to panel (a) and the black thick line is used for the sources classified as extended in both filters, corresponding to the panel (b). The thin magenta line and the shaded blue histograms refer to the sources shown in panels (c) and (d) of Fig. 3. Labels in the figure follow the order of the histograms from top to bottom. The arrow indicates the magnitude at which we expect the Tip of the RGB for a stellar population with metallicity $Z = 0.008$, and a distance modulus of 27.7.

In Fig. 3 we plot the CMD of these four kinds of sources. In panel (a) we plot the CMD for sources that are stellar in both J and Z; here the stellar population of NGC 253 is clearly visible at magnitudes fainter than $J \sim 20$, with the vertical plumes of foreground stars superimposed. In panel (b) we plot the CMD of sources extended in J and Z. This CMD is very different from that in panel (a), suggesting that the majority of the sources classified as extended in both filters are background galaxies. The CMDs shown in panels (c) for the objects that are stellar in J and extended in Z, and in (d) for objects extended in J and stellar in Z contain mostly faint sources, whose light distribution has lower S/N. In Fig. 4 we show the luminosity functions (LF) of the four kinds of sources. It appears that objects with the same morphological classification on the J tile have a similar magnitude distribution. In particular, the LFs of the sources classified as stellar on the J band image (plotted in red and magenta) present a discontinuity at $J \approx 22.5$ where the Tip of the RGB is expected if a distance modulus of 27.7 is applied to the Padova isochrones. We then conclude that most of the sources in panel (c) of Fig. 3 are likely stars, and they appear extended on the Z image because of the worse seeing. Differently, most of the sources in panel (d) are likely to be compact background galaxies.

Because NGC 253 is undergoing a starburst, we consider the presence of (young) globular clusters in our area. In panel (a) of Fig. 3 we show the evolutionary track appropriate for a globular cluster of $10^5 M_{\odot}$ with metallicity similar to that of the LMC; for a solar metallicity, such path would be shifted to redder colours by ~ 0.15 mag. While it is possible that some clusters are present in the CMD of the stellar sources, confused among the fore-

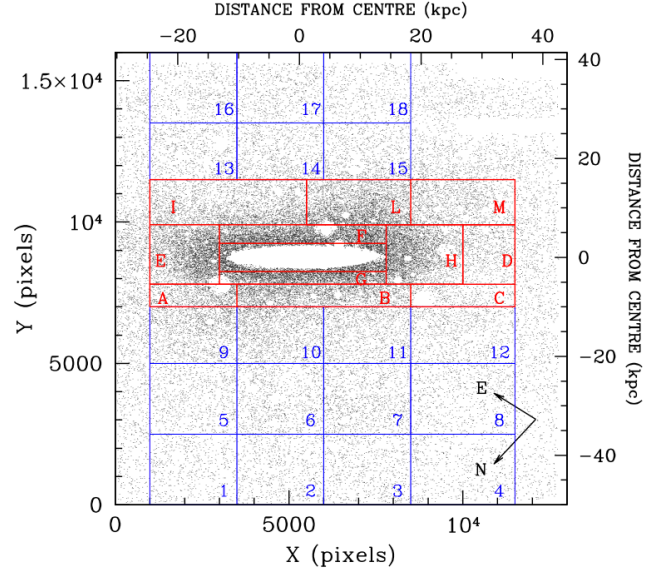


Fig. 5. Spatial distribution of catalogue A stars on the VISTA tile (J band) oriented along the detector coordinates. The upper and right axis are labelled with physical coordinates in kpc centred on the galaxy centre. Holes are clearly visible in the spatial distribution. These are due to the masking of bright foreground stars. The inner part of the disk has also been masked, because source crowding prevents accurate photometry on our images. In the upper right corner, two white rectangles show other regions with defects, where the photometry could not be performed. The cumulative area of the masked regions is a small fraction of the total surveyed area. Solid lines show the rectangular sub-regions into which we divide the tile to draw the spatially resolved CMDs shown on Fig. 11 and Fig. 19. The sub-regions are drawn so as to sample a statistically significant population of stars, and are identified with progressive numbers and letters, for the halo and the disk regions respectively.

ground stars, the CMDs of extended sources in both bands are very unlikely to contain young and blue (globular) star clusters. Indeed, we do expect globular clusters to appear as stellar-like sources in our image, because the median effective radius of Milky Way Globular Clusters is 3.2 pc (Harris 1996), which corresponds to $\sim 0''.2$ at the distance of NGC 253, well within the seeing disc.

In what follows, we consider as bona fide stars the sources classified as stellar in both filters, and whose CMD is plotted on panel (a); this is our catalogue A. However, a fair fraction of the sources classified as stars in J and extended in Z could be stellar members of NGC 253 also. We take these sources into account when discussing the halo of the galaxy, its extension and shape. We refer to the cumulative catalogue as catalogue B.

3. The Colour-Magnitude diagram of stellar sources in NGC 253

Fig. 5 shows the spatial distribution of catalogue A stars. An extended stellar disk is easily identified at $1000 \lesssim X \lesssim 11000$, $7000 \lesssim Y \lesssim 11000$, behind a sheet of foreground stars and unresolved background galaxies. The disk of the galaxy falls in the upper left section of the tile, with the centre located at $X \approx 5300$, $Y \approx 8750$. Therefore we probe the galaxy disk up to a

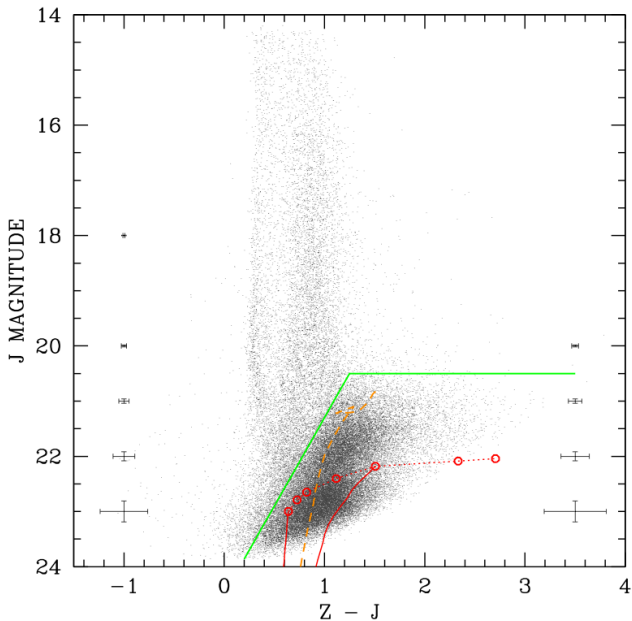


Fig. 6. CMD of catalogue A stars with theoretical loci superimposed. The models are computed with the CMD tool at stev.oapd.inaf.it/cmd and shifted by a distance modulus of 27.7. Open circles, connected with a dotted line, show the location of the RGB Tip of 10 Gyr old isochrones with metallicity $Z=(0.0001, 0.0004, 0.001, 0.004, 0.008, 0.019 \text{ and } 0.03)$, falling, respectively, at $J=(23, 22.79, 22.65, 22.4, 22.18, 22.09 \text{ and } 22.04)$. Solid thick red lines show the RGB portion of 10 Gyr old isochrones with $Z=0.0001$ and $Z=0.008$; the dashed orange line shows a 1 Gyr old isochrone with $Z=0.008$. The green solid line shows the boundary below which most stellar sources are likely members of NGC 253 (see text). 1σ error bars are shown for two values of the star’s color: those on the left refer to $J - Z = 0.5$, while those on the right to $J - Z = 1.2$ mag.

distance of more than 40 kpc along the major axis (South-West direction), and the halo up to a distance of ≈ 50 kpc, along the minor axis (North-West direction). The inner part of the disk has been masked and shows up as white region on the figure. Few very bright foreground Milky Way stars are also visible as white “holes”. Two rectangular white stripes in the upper right corner are due to the lower sensitivity of detector 16 (Sec. 2.2), and this region is not considered in the further analysis. The distribution of the stars on the disk appears asymmetrical, with an excess of sources on the upper/right side of the disk. This is the well known *southern shelf* already recognized in the literature (Beck et al. 1982; Davidge 2010; Bailin et al. 2011). Some other distortions of the disk may be recognized (e.g. on the left side of the disk along the North direction), but it is difficult to assess their reliability in this figure due to the foreground contamination.

The CMD of the bona fide stars (catalogue A) is shown in Fig. 6, superimposed with a few theoretical loci from the Padova database, shifted to a distance modulus of 27.7. The dotted line connects the theoretical RGB Tip models of 10 Gyr old isochrones with metallicity from $\sim 1/200 Z_{\odot}$ to $\sim 1.5Z_{\odot}$. The stellar population of NGC 253 stands out from the foreground contamination as a strong enhancement of faint and red sources. The comparison with the evolutionary models reveals that our CMD contains a bright RGB component plus an AGB component extending beyond the RGB Tip (i.e. $J \lesssim 22.5$). The colours

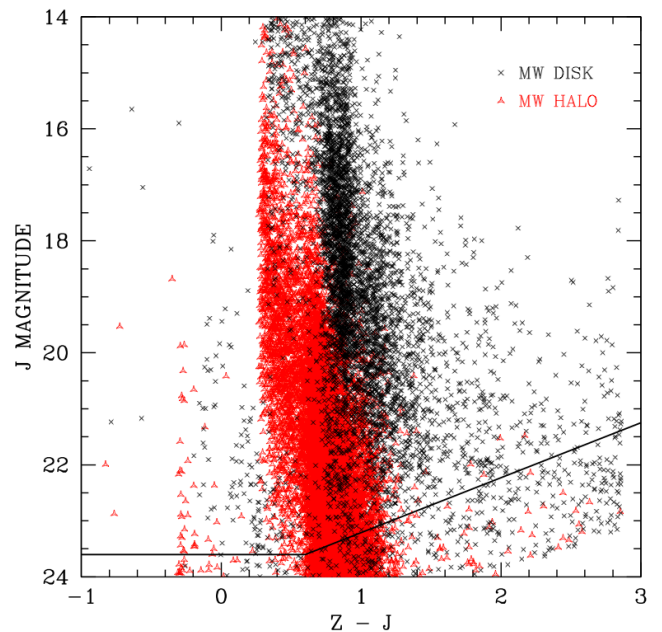


Fig. 7. CMD of the expected foreground stellar population as derived from the TRILEGAL simulation. The colour and point type encode the Milky Way component, as labelled. The solid line mimics the faint limit of the observed CMD of NGC 253. The simulation has been calculated for a 1.46 deg^2 FoV centred at the Galactic coordinates: $l = 97.37, b = -87.96$, adopting a Chabrier IMF, and keeping all other parameters at their default values.

of the RGB stars cover a wide range due to a combination of a metallicity spread and photometric errors. Using WFPC2 V and I data of a halo field of this galaxy Mouhcine et al. (2005b) measured a metallicity distribution ranging from $[\text{Fe}/\text{H}] \sim -2.3$ to $[\text{Fe}/\text{H}] \sim -0.2$. The overplotted 10 Gyr isochrones (Fig. 6) show consistency between our data and this metallicity range, taking into account the photometric errors. The luminosity extension of the AGB component indicates the presence of intermediate age (~ 1 Gyr old) stars.

The CMD in Fig. 6 shows where the stellar members of NGC 253 are located. This is the region below the solid green line. The rest of the CMD is dominated by the foreground component, and some contamination will also be present in the selected region. In the next section we assess the contribution from the Milky Way (MW) stars.

3.1. Foreground contamination: the TRILEGAL model

In spite of the high Galactic latitude of NGC 253, the shear size of our field and its photometric depth provide a large population of MW foreground stars. This component may be estimated from the stellar counts at the edges of the tiles, but since we do not know how extended the halo of NGC 253 is, and measuring its radius is one goal of the current project, we first evaluate the foreground contribution in an independent way. Fig. 7 shows the CMD of a simulated population of foreground stars as obtained using the TRILEGAL tool version 1.5² (Girardi et al. 2005) for a field with an area of 1.46 deg^2 centred on the Galactic coordinates of NGC 253. The foreground population

² stev.oapd.inaf.it/cgi-bin/trilegal

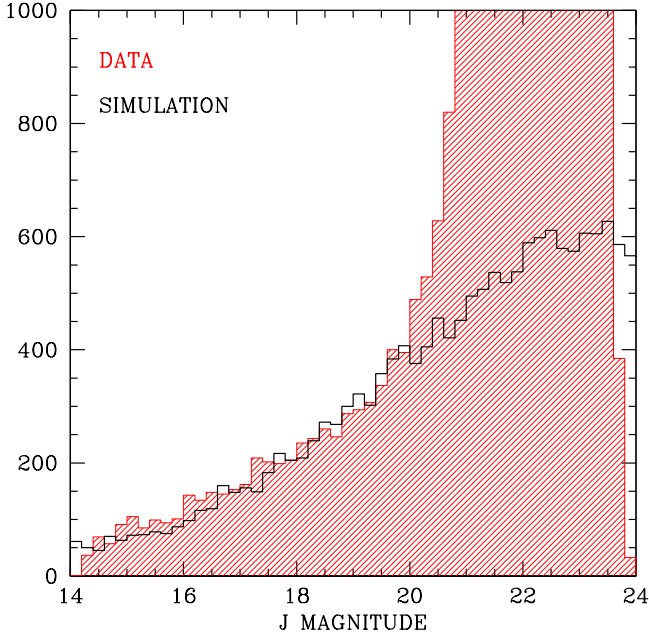


Fig. 8. Luminosity function of the expected foreground stellar population shown in Fig. 7 (black line) from the TRILEGAL simulation compared with the data (red shaded histogram). No scaling factor has been applied to bring the model and the data into agreement.

consists of a disk plus a halo component which, according to the simulation, contribute respectively 36% and 64% to the total foreground counts within the CMD region considered here (i.e. $-1 \leq (Z - J) \leq 3$; $14 \leq J \leq 24$). The great majority of model stars in Fig. 7 are Main Sequence objects with mass up to $\sim 1 M_{\odot}$, except for the bluest points ($Z - J \lesssim 0.5$) which are white dwarfs; the red tail of objects at $Z - J \geq 1.2$ are disk red dwarfs with masses between 0.07 and $0.15 M_{\odot}$. Fig. 8 shows the luminosity function of the simulated foreground population. The agreement with the observed counts at $J \lesssim 20$ is remarkable, given that this simulation is not a fit to our data, and the TRILEGAL default parameters were calibrated on different data sets. At fainter magnitudes the observed star counts exceed the simulated ones. While there is no guarantee that the model is correct at these faint magnitudes, which are poorly constrained from observations, the strong excess in our observed luminosity function sets in at a magnitude consistent with the expectation for bright stars at a distance of NGC 253.

To constrain the brightest magnitude at which the NGC 253 members are found, we compare the colour functions of the TRILEGAL simulated MW stars to the data in different magnitude bins in Fig. 9. For magnitudes brighter than $J \sim 20$ the TRILEGAL MW model and the data are in very good agreement, considering also that the synthetic diagram does not include any photometric error, which would widen the model distributions. In fact, the good agreement between the TRILEGAL model and data, in Fig. 8 and 9, confirms that our photometry is quite accurate for stars brighter than $J \approx 20$, as shown also by the small error-bars in Fig. 6. In the range $20.5 < J < 21$ the data show a strong excess of red stars compared to the model, and some excess is possibly present also in the range $20 < J < 20.5$. Therefore, we consider the location $J = 20.5$ as the upper limit to the apparent luminosity of the NGC 253 stellar members; be-

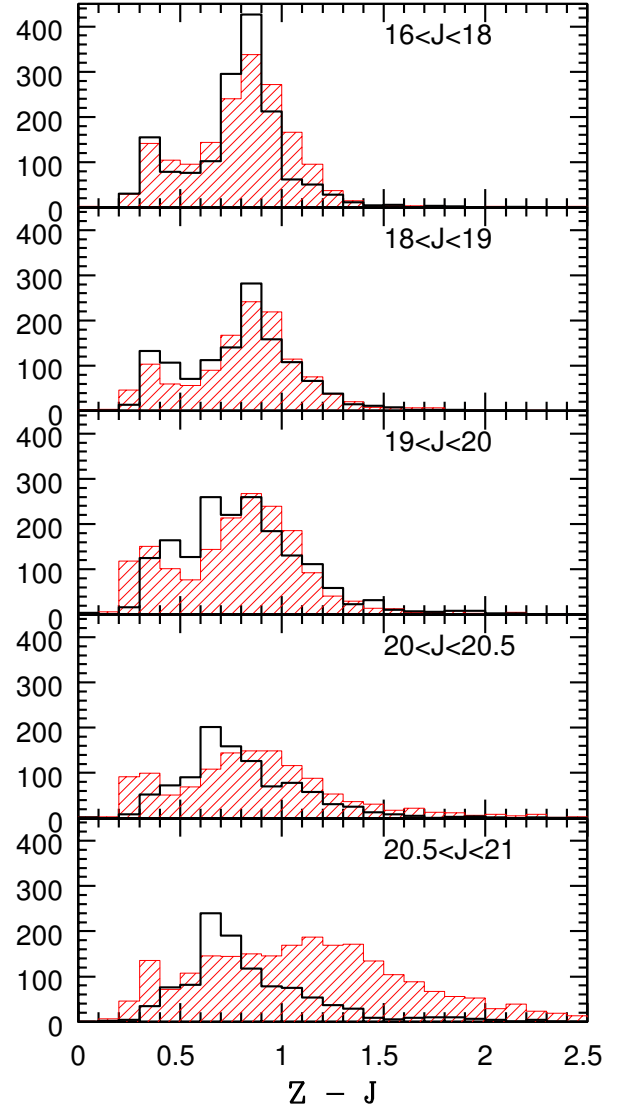


Fig. 9. Colour functions in the indicated magnitude ranges. The red shaded histograms are computed from the data in catalogue A; the solid black lines show the expected foreground stellar population as computed using TRILEGAL, see Fig. 7.

low this limit the foreground contamination is still present, but it affects mostly the blue end of the colour distribution. The solid green line in Fig. 6 shows our adopted selection to isolate bona fide stellar members of NGC 253 on the CMD. The validity of our choice is further strengthened by the cumulative distributions shown in Fig. 10, where stars brighter than $J = 20.5$ closely follow the uniform distribution on the tile, as expected for the Milky Way foreground. Conversely, stars below this locus on the CMD (RGB and AGB) are concentrated towards the disk of NGC 253.

3.2. The CMD of NGC 253 star members

The selection criteria defined in Section 3.1 for the stellar population in NGC 253 can be used to verify whether there are sub-regions in the tile where this population is scarce or absent

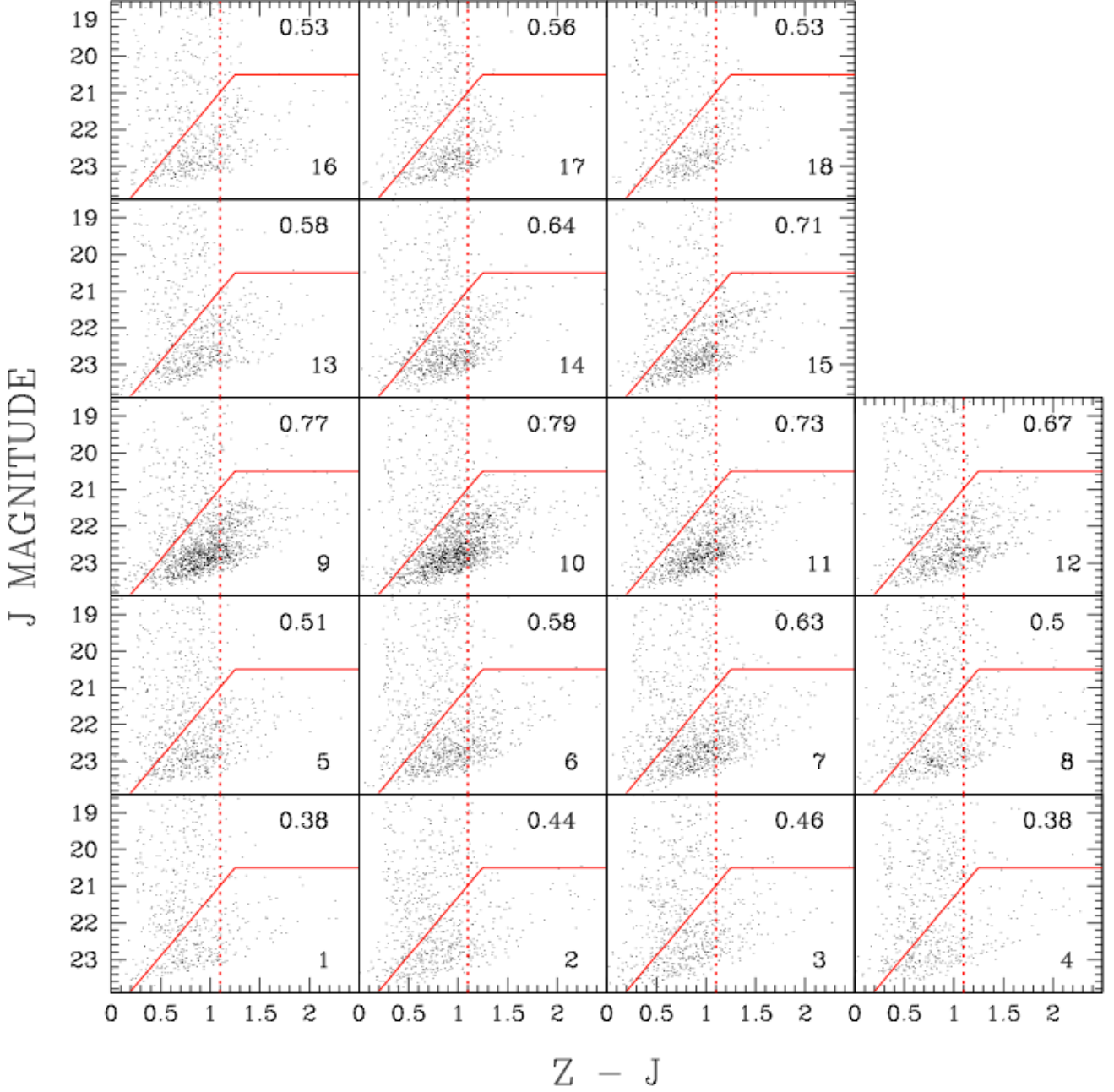


Fig. 11. Spatially resolved CMDs over the VISTA tile (halo regions). Each panel shows the CMD of the stars falling in a rectangular sub-region labelled in the bottom right corner with the same number as in Fig. 5. The solid line shows the dividing line of the likely members of NGC 253, as in Fig. 6. The number in the upper right corner is the ratio between the stars below this envelope and the total number of stars in the selected region of the tile. Notice that the CMDs are plotted only up to $J = 18$, while stars are measured up to $J = 14$. The vertical dotted line at $Z - J = 1.1$ marks the colour at which the NGC 253 stellar population greatly outnumbers the foreground contamination (see Fig.9).

and derive an empirical evaluation of the contamination by foreground stars and background unresolved galaxies.

We show in Fig. 11 the spatially resolved CMDs over the portion of the VISTA tile which maps the halo around the galaxy, i.e. for the rectangular sub-regions drawn on Fig. 5 and identified with progressive numbers. The following sub-regions are excluded:

1. $X < 1000$ and $X > 11500$ because these pixels received shorter exposures due to the pawprint sampling;
2. the region with $7000 < Y < 11500$ is dominated by the disk of NGC 253, hence it is not useful to evaluate the foreground/background contamination;

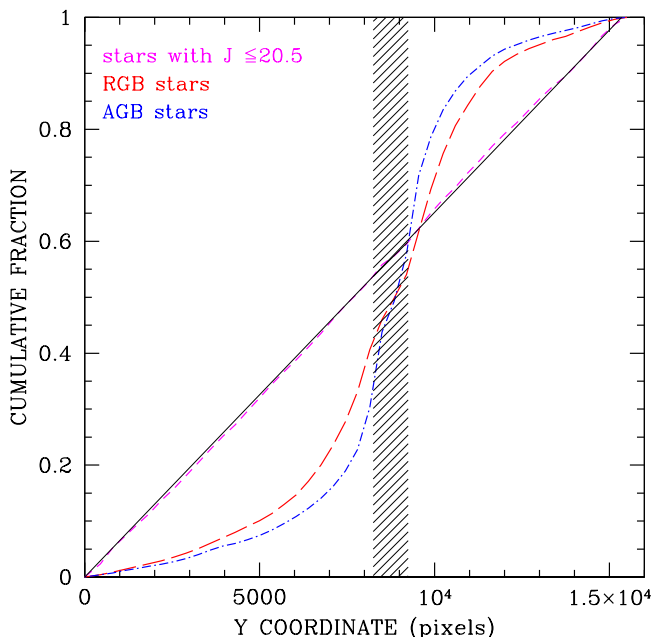


Fig. 10. Cumulative distributions along the vertical (Y) coordinate of the tile for stellar sources with different locations on the CMD. The short dashed (magenta) line refers to stars brighter than $J = 20.5$; RGB (red, long dashed) and AGB (blue, dot-dashed) stars are located below the solid green line in Fig. 6, respectively below and above the dotted red line connecting the RGB tips from evolutionary models.

- we also discard the upper right corner of the VISTA tile (at $X > 8500, Y > 11500$) because of the defects of detector 16 (see Sec. 2.2).

The sub-regions targeting the halo of NGC 253 do not have the same area because we aim at maximizing the contrast between the galaxy population and the foreground contamination. Therefore we consider wider areas in the outer portions of the tile. The solid line plotted on each CMD of Fig. 11 shows the locus below which we expect the stars members of NGC 253 to dominate, according to the discussion in Section 3.1.

The number listed on the upper right corner of each panel of Fig. 11 is the fraction of stars in the spatially selected sub-region which falls below the solid line, with respect to the total number of stars in catalogue A in the same spatial region. The vertical dotted line helps us to evaluate the contribution from the NGC 253 members, that appear as a red population and dominate the foreground/background contaminants (see Fig. 9). On Fig. 11 the number of red stars associated with the NGC 253 population increases in sub-regions closer to the disk, as also traced by the fraction of stars below the solid line.

For comparison, the TRILEGAL simulation shown in Fig. 7, has a fraction of 0.32, having taken into account the magnitude limit drawn as a solid black line in this figure. This fraction is similar to the value measured on the bottom corners of the tile, i.e. in sub-regions 1 and 4. Although the colour distribution in regions 1 to 4 and 16 to 18 may be consistent with that of the foreground population, the excess of stars below the solid line in regions 2, 3, 16, 17 and 18 suggests that a component of NGC 253 members is likely present in these sub-regions.

Actually, the detailed comparison of the stellar population in sub-regions 1+4 with the TRILEGAL model, suitably re-scaled by the ratio of the sampled areas, shows a remarkable match of the luminosity function and color distribution at $J \lesssim 20.5$, but still there is an excess at faint magnitudes. Since the model does not include the contribution of the background unresolved galaxies (and may have uncertain calibration at these faint magnitudes as mentioned above), we prefer to rely on the empirical estimate of the foreground+background contamination using sub-regions 1+4 ($1000 \leq X \leq 3500; Y \leq 2500$ plus $8500 \leq X \leq 11500; Y \leq 2500$). There are 621 and 683 stellar sources in the regions 1 and 4 of the tile, respectively. The total number of sources is then 1304 over a combined (region 1+4) area of 0.123 deg^2 and the surface density of foreground stars included in our catalogue of bona fide stars, i.e. our photometric catalogue A, is empirically estimated to be 0.1×10^5 stars per deg^2 , on average. This value will be considered later, when discussing the extent of the NGC 253 stellar halo.

4. NGC 253 stellar disk and halo structure

Detailed analysis of the inner regions and of the disk structure in NGC 253 is presented in Iodice et al. (in prep.). Here we discuss primarily the structure of the halo, but to do that we need to know how extended the disk is, and where the disk-halo transition occurs. Since NGC 253 is not perfectly edge on, we must evaluate how far the disk projects on the VISTA tile and extends along the projected minor axis. We do that assuming that the disk is circular, by measuring its extension along the major axis and then projecting it along the minor axis using the inclination angle of the disk.

4.1. The stellar disk

In Fig. 12 we show the stellar density profile along the two sides of the major axis (open and filled circles), which turn out to be quite smooth and symmetric. The solid line shows the counts of the NGC 253 bona fide members along the South-West direction, while the dashed line shows the profile along the North-East direction. The profiles from catalogue B show very similar trends.

When the South-West and North-East semi-major axis number density profiles are plotted on top of each other as in Fig. 12, a change in the radial slopes appears at a distance of approximately 25 kpc from the centre. The South-West profile is more extended than the North-East one, because the galaxy is not centred in the tile (the disk centre is at $X=5300, Y=8750$ coordinate). We interpret the change of slope at ~ 25 kpc as signalling the location of the outer edge of the disk. This interpretation is prompted also by the analysis of the surface brightness profile of the entire disk in Iodice et al. (in prep.). Since the inclination of NGC 253 is approximately 76 deg, the projected component of the disk along the minor axis is ~ 6 kpc, corresponding to ± 1000 pix from the disk plane. This implies that the regions of the tile at $Y < 7500$ and $Y > 10000$ in Fig. 5, do not include stellar populations from the circular thin disk. However, we know that the disk of NGC 253 appears quite disturbed, hence those regions of the tile closer to its edge may likely include some extra-planar stellar component from the disk.

Fig. 13 shows the complete radial profile along the major axis of NGC 253 out to 40 arcmin, i.e. 40.3 kpc, constructed by combining two surface brightness profiles (small coloured dots) extracted along North-East and South-West major axes in the J -band images with the number density from the J -band star counts corrected for crowding effects (black dots with error

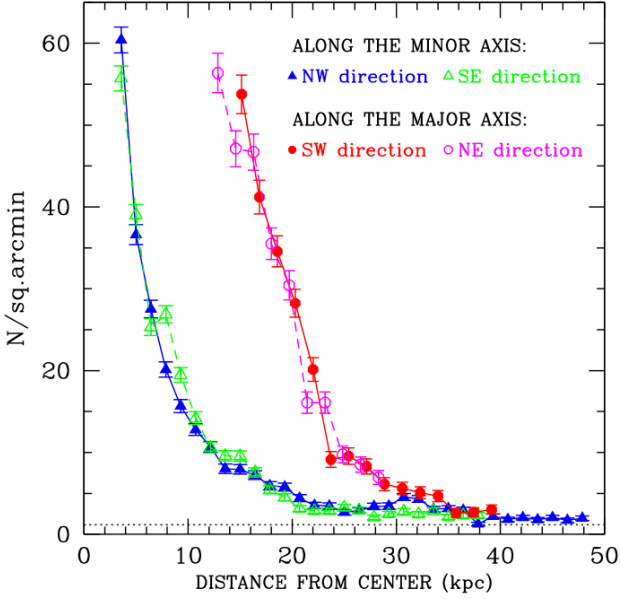


Fig. 12. Surface density profiles along the major and minor axis of the NGC 253 disk, as labelled. The profiles are constructed from catalogue A, considering only probable members of NGC 253 (stars below the solid line in Fig. 6), and the error bars show the $\pm 1\sigma$ Poissonian uncertainty. The star counts along the major axis are performed within a horizontal stripe defined by $8250 \leq Y \leq 9250$ pixels, corresponding to a width of ≈ 5.7 kpc. The central region is excluded due to crowding. The minor axis profiles are extracted from a stripe at $3800 \leq X \leq 6800$ pixels. At a distance of ≈ 35 kpc from the centre the number density is nearly the same in the two orthogonal directions. The dotted black line shows the density of foreground/background objects measured on sub-regions 1+4 in Fig. 11 in the same selected part of the CMD.

bars), following the prescription described in Irwin & Trimble (1984). *J*-band surface brightness profiles were extracted from an earlier commissioning image, in which the NGC 253 disk was aligned at 90 degrees with respect to the science verification tile, hence sampling different regions of the pawprint mosaic. These data turned out better suited to measure the faint surface brightness in the outer regions of the disk because of a more accurate measurement of the background. The average of the two *J*-band surface brightness profiles is shown by the light blue dots in Fig. 13. The surface brightness and the number density profiles were extracted using the same projected regions relative to the major axis, a rectangular strip 4 arcmin wide beyond a radius of 10 arcmin but tapering linearly to 1/2 arcmin at the centre, to better sample the central regions.

The profiles along the North-East and South-West directions are extremely similar out to ~ 16 arcmin and trace a well defined exponential decline, with a scale length of 2.1 kpc. Beyond this distance the surface brightness is affected by a large error due to background artefacts at the level of roughly 1 ADU caused by the complex processing. The profile from the star counts has been derived applying a correction for crowding based on the seeing affecting the data so that we could get a (small) overlapping region between the profiles computed in these different ways. Notice that the corrected counts nicely follow the same

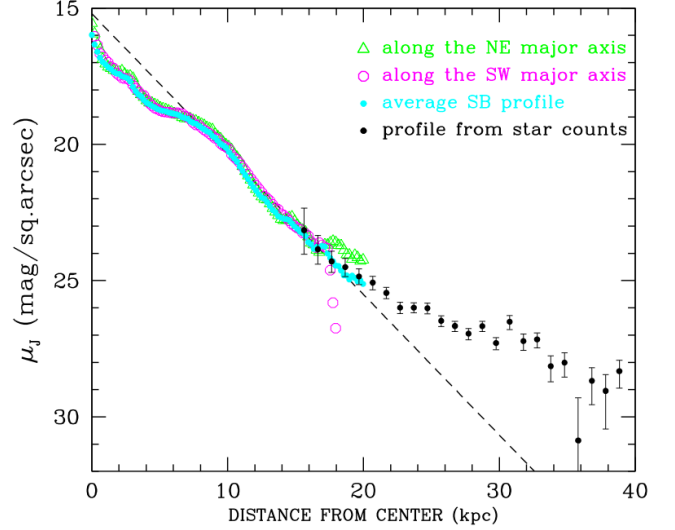


Fig. 13. Composite surface brightness profile along the major axis of NGC 253. The green triangles and magenta circles show surface brightness profiles extracted along the North-East and South-West major axes directions from the *J*-band early commissioning data. Light blue small dots trace the average *J*-band surface brightness profile. Small black dots are the number density profile of star members of NGC 253, corrected for crowding effects, and scaled to the surface brightness profile between 15-18 arcmin from the center. The error bars are Poissonian from counts and also include the foreground/background estimated errors. The dashed line (not a fit) helps to better see the continuity of the surface brightness and scaled number density profiles.

exponential slope as the surface brightness profile in the innermost (between 16 and 18 arcmin) region, but becomes flatter at distances larger than about 20 arcmin, (~ 20 kpc), indicating the transition between the disk and the halo component of NGC 253. The uncertainty in the sky background subtraction, which affects the surface brightness profile at $d \gtrsim 16$ arcmin, and that on the crowding correction, which affects the counts at $d \lesssim 18$ arcmin, implies some flexibility when matching the two components. This reflects on the slope of the matched profile and, consequently, on the positioning of the slope change. With our data we constrain the disk size of NGC 253 to a range between 20 (Fig. 13) to 25 kpc (Fig. 12); further analysis of the disk structure is presented in Iodice et al. (in prep.). We note that a disk size of ~ 20 kpc is consistent with what measured in other galaxies (Ibata et al. 2013).

In order to match the star number counts to the surface brightness profile in Fig. 13 the plotted function is:

$$f = -2.5 \log N/A + 21.4 \quad (3)$$

where N/A is the surface density of crowding corrected stellar counts per square arcsec. The value of 21.4 which is needed to bring into agreement the surface photometry with star counts can be translated into the number of detected stars per unit luminosity of the parent population, which turns out to be $N/L_J \approx 10^{-4} L_{J,\odot}^{-1}$. This number compares well with the theoretical expectations. For the two simulations described in Greggio et al. (2012) the number of stars brighter than $M_J = -4.2$ (which corresponds to $J=23.5$ for NGC 253) is $N_{\text{sim}}/L_J = 7 \div 9 \times 10^{-5} L_{J,\odot}^{-1}$ respectively for a constant star formation rate over the last 12

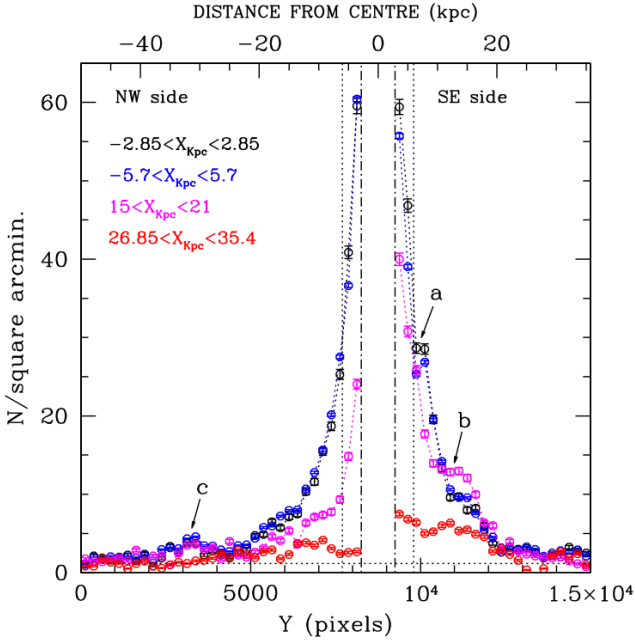


Fig. 14. Surface density profiles for the catalogue A likely members of NGC 253 (selected as in Fig. 12) along directions parallel to the minor axis within four stripes as labelled. Dot-dashed lines limit the central region of the tile, where photometry is affected by very high crowding. Dotted lines are drawn at ± 6 kpc from the galaxy major axis, showing the projected extension along the minor axis of the (circular) disk of the galaxy. Regions outside to the dotted lines should not be dominated by stars from the thin disk component. The horizontal line shows the level of the foreground/background contamination as in Fig. 12. The arrows highlight the high density regions described in the text.

Gyr, and for an old (~ 11 Gyr) episode of star formation. The empirical scaling that we determine from the comparison of the two profiles is thus in good agreement with the predictions of stellar evolution theory.

4.2. The halo structure and substructure

In Fig. 12 we directly compare the profiles along the minor and major axes. Although the disk dominates most of the stripe along the major axis, the profiles along the two orthogonal directions seem to converge to the same level at ~ 30 kpc from the centre. This is fortuitous and due to the excess counts in the North-West profile (shown in blue) corresponding to an overdensity in the halo discussed below. Rather, the profiles along the major and minor axes become remarkably close at distances $\gtrsim 35$ kpc from the centre. The similarity in the values for the number density at these distances along the two orthogonal axes, and their excess above the foreground/background level suggests that the halo component dominates at $R > 35$ kpc and that it is nearly spherical.

In Fig. 14 we plot the stellar density profiles obtained from star counts computed in four stripes parallel to the minor axis and indicated on Fig. 15. The blue and black lines refer to two central stripes that include the minor axis with two different widths. At the distance of NGC 253 they are 5.7 and 11.4 kpc wide. Notice that the profile in blue is the same minor axis pro-

file as in Fig. 12. The steep radial decrease of the stellar density on the central stripes does not depend on the width of the stripe; the two profiles fall virtually one on top of the other, indicating that the distribution is rather uniform along the X direction.

At $Y \approx 10000$, i.e. at ~ 7 kpc from the galactic plane in the South-East direction, the surface density in both central stripes shows an enhancement labelled *a*, which does not have a symmetric counterpart on the other side at $Y \sim 7500$. In Fig. 5 we identify a very bright foreground star located at $X \approx 6000$, $Y \approx 9800$ that may be affecting the profile. However, the profile in black, extracted from the stripe $4800 \leq X \leq 5800$, does not include this star, and still shows the local density enhancement at the same distance from the plane. Therefore we attribute this high density structure to the *southern shelf* (Bailin et al. 2011). The southern shelf feature is responsible for a second overdensity that is measured at a distance of 18 kpc from the minor axis, and in the stripe centered at a distance of 18 kpc from the minor axis. This second overdensity is labelled as *b* and corresponds to the enhancement of stellar sources on Fig. 5 to the south of the disk. In the stripe at 18 kpc from the minor axis, stars associated with the southern shelf can be traced from ~ 9 kpc to ~ 15 kpc (projected distance) above the disk.

The lowest curve (in red) on Fig. 14 refers to a density profile extracted from a stripe which is far from the minor axis of the galaxy, centred at ≈ 31 kpc. The steep rise of the star counts when approaching the disk of the galaxy is not detected at this location, but we notice a density enhancement on the south-east side that may correspond to the southern shelf. In that case the southern shelf overdensity is traced up to a ~ 35 kpc distance from the centre of the galaxy.

On the North-West side of the tile there is a modest overdensity at ~ 30 kpc below the galaxy plane ($3000 < Y < 3500$), labelled *c* in Fig. 14, that is consistently traced in three stripes, black, blue and magenta. On the tile this looks like a filamentary substructure located at ~ 28 kpc from the plane of the galaxy, and extending for about 20 kpc. All these features are also clearly detected on catalogue B and this supports their reliability.

In order to visualize the southern shelf and the overdensity at 28 kpc below the plane of the disk we compute the contours of the density of stellar sources from catalogue A. These isodensity contours are computed following the method described in Goldsbury et al. (2010). This method is in general used to perform a fit of ellipses (or circles) to the internal isocontours in order to derive an accurate centre for stellar components. Here we use it to study the shape of the disk and inner halo of NGC 253 and to investigate the possible presence of overdensities. The first step is to construct a grid of 200×200 resolution elements with a size of 100×100 pixels each. Then, the number of stars found within a circle of 200 pixels in radius, centred on each box of the grid, corresponds to the density level at each given element of our grid. Finally, we draw the contours by connecting the grid boxes of equal density. In Fig. 15 the outermost isodensity contour has 0.23×10^5 stars per deg^2 ; we remind that the density of the background (Milky Way foreground stars + unresolved background galaxies) as estimated empirically in Section 3.2 amounts to 0.1×10^5 stars per deg^2 .

The disk of the galaxy is traced very neatly by elliptical contours, with some irregularities due to the presence of very bright foreground stars – the most conspicuous being one bright star on the south east side ($X = 6075$; $Y = 9790$) and two on the northwest ($X = 3080$, $Y = 7750$; $X = 8880$, $Y = 7235$). The *southern shelf* is clearly visible as an elongation of the contours in the upper right part of the disk, and there seems to be a sim-

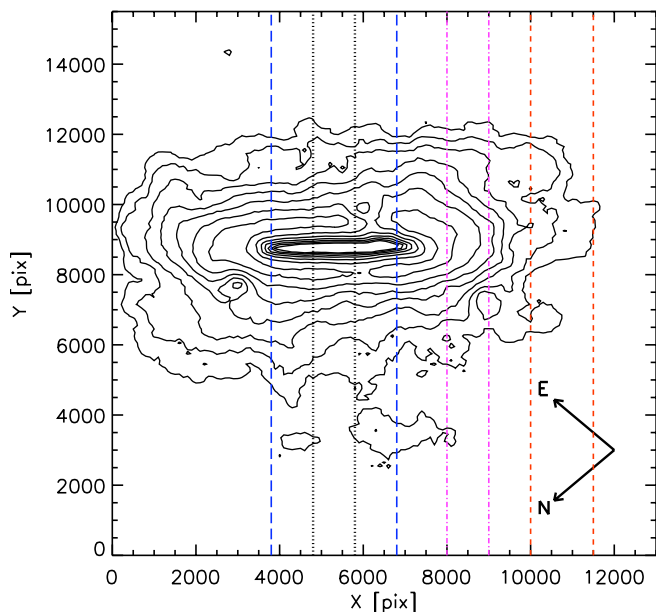


Fig. 15. Isodensity contour levels for sources classified as stellar on both *Z* and *J* tiles, i.e. catalogue A. Contours are plotted so that, going towards the inner regions, each contour has a 40% higher density with respect to the previous one. The outermost contour has a density of 0.23×10^5 stars/deg²; the next has a density of 0.32×10^5 stars/deg² and so on. The vertical lines indicate the regions along the minor axis on which the profiles in Fig. 14 are computed.

ilar feature in the lower left part of the disk: i.e. an elongated structure in the north direction. This portion of the galaxy was marginally included in the WIRCam images of Field 1 analyzed by Davidge (2010), (see Fig. 1), but the elongation of the spatial distribution of the stars can be appreciated only with the large field of view and much deeper photometry of our VISTA tile.

The contours for the number counts appear very flattened in the innermost portion of the stellar distribution, with a projected axial ratio of ~ 0.2 ; this ratio corresponds to the disk inclined at 76 degrees. The axial ratio tends to increase going towards the outer parts, but the shape remains elliptical up to the lowest density level that we trace. For example, on the fourth outermost contour in Fig. 15 we estimate $b/a \approx 0.4$, in agreement with Bailin et al. (2011). The inner halo is thus elliptical, as expected for the dark matter halos around galaxies based on the cold dark matter simulations (Helmi 2004), and similar to what is observed for the halos of the Milky Way and Andromeda (Bell et al. 2008; Ibata et al. 2007). We identify the over density at $Y = 3000$ extending from $X = 6000$ to $X = 8000$, which is linked to the over density at $X \sim 4000$ at the same Y coordinate. This corresponds to the overdensity labelled as *c* in Fig. 14 and supports the claim that we have detected a substructure at this location.

This substructure in the halo is particularly evident in the map in Fig. 16, which was created from a 512×512 grid of star counts over the tile. The smoothing to a resolution of $1/2$ arcmin is applied to highlight the presence of the low surface brightness structure to the North-West of the main body. Furthermore this map emphasizes the overall shape and warp/distorsion of the outer disk/halo. Our images are not deep enough to allow a

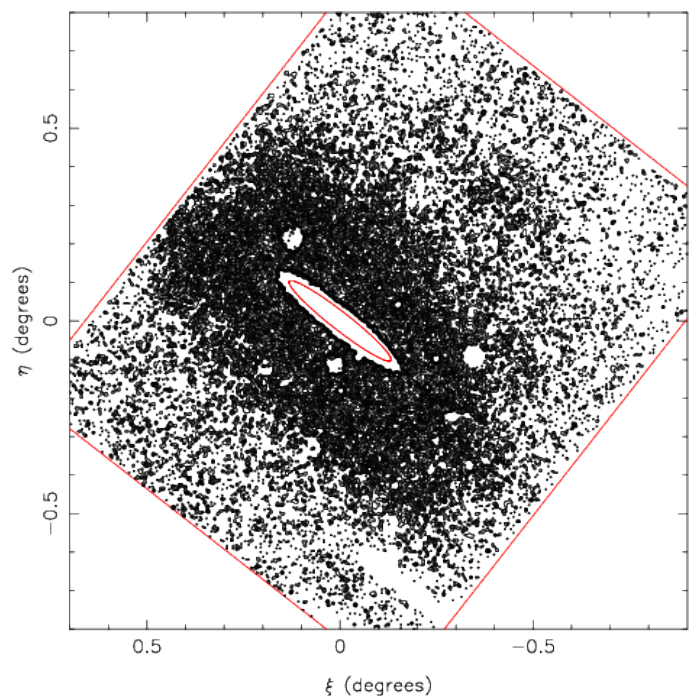


Fig. 16. Map of catalogue A stellar like sources smoothed to a resolution of $1/2$ arcmin. The orientation of the map is N to the top and E to the left and the outline of the tile footprint is shown in red.

robust assessment of the geometry of the halo beyond the outer edge in Fig. 15, but the matching surface density profiles along the minor and major axis beyond ≈ 35 kpc (Fig. 12) hints at a rounder outer halo.

5. The Star Formation History

We derive information on the star formation history of the stellar populations in NGC 253 by comparing the observed CMD with theoretical isochrones for different ages and metallicities. To do that we first clean the CMD in Fig. 6 to remove the contribution due to foreground stars and background compact galaxies. The statistical decontamination is performed by assuming the CMDs of regions 1 + 4 (see Fig. 11) as foreground+background templates and scaling their star's distribution by the ratio of surveyed areas. The template CMD is then statistically subtracted from the total observed CMD by removing from the latter the appropriate number of stars with similar colour and magnitude. The subtraction is done star by star, picking up a random star within the error ellipse, which then gets removed from the observed CMD (Zoccali et al. 2003). We experimented with several decontamination runs, with different random number seed and slightly different error ellipse, in order to determine the robustness of the result. Figures 17 and 18 show such decontaminated CMD with superimposed young and intermediate age isochrones from the Padova database³. The isochrones are based on the Marigo et al. (2008) set of tracks, for a metallicity of $Z=0.008$.

The isochrones on Fig. 17 have ages between 10 and 100 Myr, and are plotted so that the density of points indicates the sections of the isochrones where stars are more likely to be located. On this figure, the black line limits the region where stars

³ Isochrones are computed using the CMD tool available from <http://stev.oapd.inaf.it/cmd>

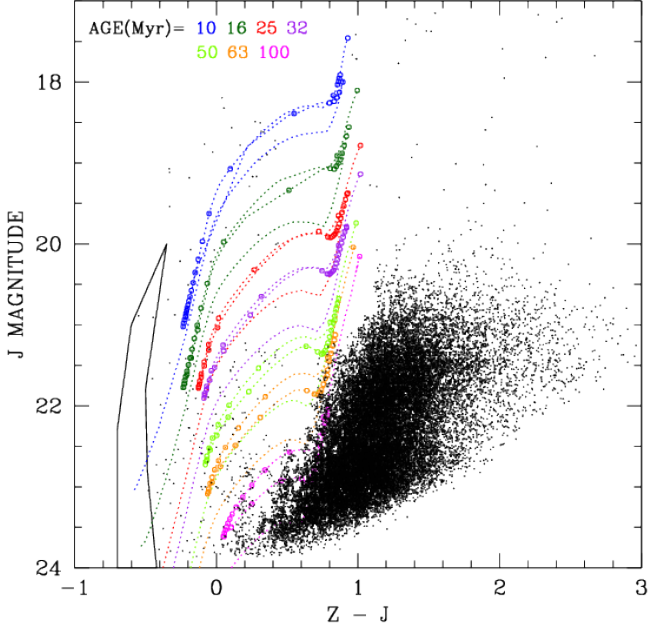


Fig. 17. Statistically decontaminated CMD for catalogue A with theoretical isochrones superimposed. The solid black line limits the region of the main sequence (MS) stars, while the dotted lines connect the isochrones of the post-MS evolution for different ages, i.e. for 100, 63, 50, 32, 25, 16 and 10 Myr (from bottom to top). The open circles show the position of 30 models equally spaced in evolutionary mass between the turn-off mass and the mass of the dying star. The density of these circles is thus proportional to the lifetime of the evolutionary sub-phase and indicate where the stars are more likely located.

on the main sequence and with ages younger than ~ 15 Myr should be found. Since we count (almost) no stars in this region, we conclude that there was very little (if any) star formation in the very recent past in the outer disk and halo of NGC 253. Ongoing star formation has been detected in NGC 253 (Engelbracht et al. 1998; Comerón et al. 2001; Ott et al. 2005; Radburn-Smith et al. 2011), but mostly in the inner regions of the disk, which are too crowded for our photometry.

After the statistical subtraction of foreground stars and background compact galaxies, there are no stars left in the red supergiant region, at ($J \lesssim 20.5$, $Z - J \approx 0.8$). This implies that there are (virtually) no red helium burning stars with ages between 10 and ~ 50 Myr. Some stars (at $Z - J \lesssim 0.2$) populate the cleaned CMD in the region of the blue portion of the core helium burning loops in this range of ages. However, their spatial distribution is rather scattered, and the lack of their “red” counterpart further weakens the interpretation of these objects as blue loop stars. Core helium burning stars with ages between 50 and 100 Myr may be present in the CMD; those in the red section of the loop would be found at the blue edge of the AGB/RGB angle, those in the blue section of the loop would be located at $J > 22$ and ($Z - J$) ~ 0.2 . However, the spatial distribution of these potential blue loop giants does not show any concentration towards the disk of NGC 253 or association with substructures. All stars with $Z - J \lesssim 0.2$ appear distributed at random on the tile. We conclude that they are most likely noise associated with the sta-

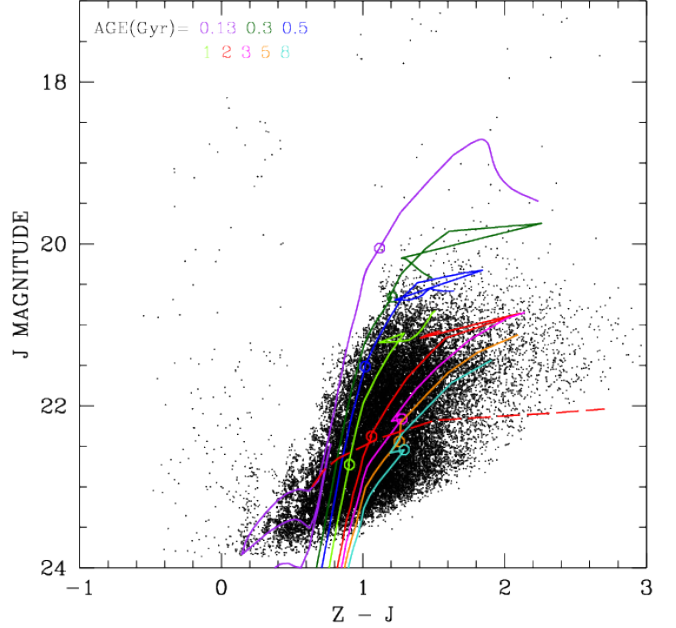


Fig. 18. Statistically decontaminated CMD for catalogue A with $Z=0.008$ isochrones superimposed. Isochrone ages are 0.13, 0.3, 0.5, 1, 2, 3, 5, and 8 Gyr from the bluest to the reddest one. The dashed line connects the tip of the RGB stars of the 10 Gyr old isochrones with metallicity from $Z=0.0001$ to $Z=0.03$. The open circles mark the model at the first thermal pulse.

tistical subtraction of foreground stars and background compact galaxies from the observed CMD.

The comparison of the CMD with solar metallicity isochrones leads to similar results; young main sequence stars are absent, as well as giants at the blue edge of the blue loop which should populate a vertical stripe at $Z - J \approx 0.3$. We conclude that star formation was virtually quiescent over the last 100 Myr in the outer disk and halo components of NGC 253.

Fig. 18 shows the comparison between the statistically decontaminated CMD and isochrones with ages between 0.13 and 8 Gyrs, which encompass well the distribution of our data. These isochrones come from the same dataset as those in Fig. 17, and have a metallicity of $Z=0.008$. We considered lower and higher metallicity models, but found that these provide a worse match to the measured colours, the former being too blue and the latter too red with respect to the stars sampled by our CMD. The dashed line in Fig. 17 shows the position of the tip of the RGB for a wide range of metallicities (i.e. the same as the dotted line in Fig. 6). The stars brighter than the RGB tip, but fainter than $J \sim 20$, are in the AGB evolutionary phase. Comparing the position of the first thermal pulse on each isochrone (indicated with a circle) to the data we conclude that most of the AGB stars on our CMD appear to be in the thermally pulsing phase. Early AGB stars may be found at the blue end of this distribution, in which case they may belong to a relatively young component. Alternatively, the blue edge of the distribution could include relatively older stars scattered to the blue by photometric errors.

There are very few stars, if any, around the youngest of the plotted isochrones in its bright section. If a conspicuous star formation episode took place between 0.1 and 0.3 Gyr ago we would sample its AGB progeny at $J \lesssim 20$, which is not there.

The upper limit of $J = 20.5$ to the NGC 253 members, discussed in the previous section, translates into a lower limit of 0.5 Gyr for the age of the most recent star formation activity in the region of the galaxy that we are investigating. Notice, however, that since some bright stars between the 0.5 and 0.3 Gyr isochrones are present in our CMD, the lower limit to the stellar ages is estimated between 0.5 and 0.3 Gyr in our surveyed region. The bright AGB population extends to very red colours, in principle consistent with ages as old as 10 Gyr, for $Z=0.008$. The red bright AGB stars, however, could also have higher metallicity and younger ages.

The number of bright AGB stars per unit mass of the parent population, hereafter the specific production of bright AGB stars (P_{AGB}), is large at intermediate ages, but becomes small at old ages, due to the action of mass loss on the relatively small envelope of low mass thermally pulsing AGB stars (Noel et al. 2013; Greggio & Renzini 2011). Using Marigo et al. (2008) models, we compute P_{AGB} in the region of the CMD brighter than the (red) dashed line on Fig. 18 from stellar populations with ages between 0.3 and 3 Gyrs. Assuming a Salpeter-diet IMF (i.e. $\phi(m) \propto m^{-1.3}$ between 0.1 and $0.5 M_{\odot}$; $\phi(m) \propto m^{-2.35}$ above $0.5 M_{\odot}$), models with $Z = 0.008$ yield $P_{\text{AGB}} = (0.8, 1.7, 1.4, 0.3) \times 10^{-4} M_{\odot}^{-1}$ respectively for ages of (0.3, 0.6, 1, 3) Gyr. The mean value of the specific production over this age range turns out to be 0.8 stars per $10000 M_{\odot}$. Since we count ~ 17000 stars in this part of the CMD, the AGB bright component traces about $2 \times 10^8 M_{\odot}$ of stars formed between 0.3 and 3.0 Gyrs ago, if the star formation rate was constant between these epochs. The stellar mass formed at intermediate ages would be different by a factor of ~ 2 if the star formation was peaked at a specific age. However, the color distribution of bright AGB stars does not support a bursting star formation history. An additional uncertainty in this mass estimate comes from systematics in the models and assumed IMF and metallicity. The evaluation of these effects is beyond the scope of this paper. Most of this star formation occurred in the disk rather than in the halo of NGC 253. We count ≈ 12500 bright AGB members of NGC 253 in the disk (specifically within $1000 \leq X \leq 9500$ and $7000 \leq Y \leq 10500$), which is close to 75% of the total detected on the tile.

Figure 19 shows the spatially resolved CMD for the section of the tile covering the outer disk of NGC 253. The sub-regions, identified with the same letter in the lower right corners as in Fig. 5, have been designed with the aim of exploring systematic variations of the CMD morphology in different parts of the galaxy. Regions A and B sample the more external portion of the disk, while regions C and D also probe the inner halo. Regions E, F, G and H target the disk; region L is centred on the southern shelf, while regions I and M sample the inner halo on two opposite sides of region L. The overall appearance of the CMD is quite homogeneous over the outer disk, with similar upper boundary and colour range covered by the stellar members of NGC 253.

The upper right corner of each panel reports two numbers. The upper number is the analog of the fraction reported in the upper right corner on each panel of Fig. 11, i.e. the fraction of NGC 253 star members over the total number of stars detected in the sub-region. This fraction increases as one approaches the disk of NGC 253, and nicely complements the trend shown in Fig. 11. The lower number is the ratio between the bright AGB stars, counted between the solid and dotted lines, and the RGB stars, counted below the dotted lines. This fraction increases markedly towards the disk on NGC 253, so that in regions F and G the bright AGB component outnumbers the faint RGB one. Part of this trend is due to the effect of crowding which makes

stars appear brighter than they are (see e.g. Greggio & Renzini 2011) and at the same time hampers detection of the faint RGB component.

The shift in the luminosity function towards the bright magnitudes artificially induced by crowding may also be responsible for the higher fraction in panels F and G of bright AGB stars close to the upper envelope (solid line). On the other hand, both the higher AGB-to-RGB ratio and the more populous upper envelope of the AGB stars could indicate a stronger star formation between 0.3 and 0.5 Gyr ago in these parts of the disk with respect to those further out. It is also plausible that the blue portion of the AGB region of the CMDs in the inner disk includes some red supergiants (see Fig. 17). This younger population is recognized in the higher spatial resolution HST data (Radburn-Smith et al. 2011), especially in the more central parts. Actually, the detailed study of the star formation history in the disk of NGC 253 can be best performed using the HST data.

Similar considerations hold for the regions of the outer disk shown in Fig. 19, i.e. we cannot state with confidence whether the observed gradient of the ratio between the bright AGB and the RGB stars reflects a real gradient of star formation, with regions B, I, L and M less active in the more recent past with respect to regions E and H, and the latter less active than regions F and G. As mentioned above, the morphology of the CMDs appears quite homogeneous, indicating similar star formation histories. Nevertheless we remark on the following differences: in region I there is a horizontal feature at $J \approx 21.5$ extending to very red colours, reminiscent of carbon giant stars (see also Davidge 2010). A similar morphology can be traced on the CMD of regions L and M, but is much less evident on the CMDs of the other regions. The CMD of region L, which is centred on the *southern shelf*, shows a wider AGB with respect to the two adjacent regions. Conversely, the AGB spans a relatively narrow colour range in regions E and B. These variations in morphology may indicate different metallicity distributions, and details of the star formation history; a quantitative analysis of the population gradient needs the computation of synthetic CMDs taking into account the detailed photometric quality of our data, which is beyond the scope of this work.

6. Summary and Discussion

We present the results based on deep Z and J band VISTA photometry of the spiral galaxy NGC 253 extending up to ~ 40 kpc from the centre along the major axis (in the South-West direction) and up to ~ 50 kpc along the minor axis (in the North-West direction), which enables the study of the stellar population associated with the outer disk and halo of this spiral galaxy.

Adopting the distance modulus derived by Radburn-Smith et al. (2011) from ACS observations, we are able to place the tip of the RGB at $J \approx 22.5$ and determine the nature of the NGC 253 members visible in our CMD plots. These appear to consist of bright RGB stars and AGB stars. The excess number counts in the CMD over the empirically estimated foreground/background trace halo star members of NGC 253 as far as 50 kpc from the centre. The spatial distribution of these excess counts leaves little room for an alternative explanation, as can be appreciated from Fig. 20, since the cumulative counts start deviating from a straight line at small Y coordinate. The uncertainty on the level of the foreground/background contamination, coupled with the relatively bright limiting magnitude of our data, prevent a robust determination of the size of the halo, but several evidences suggest that it extends over the whole tile and possibly beyond (Fig.

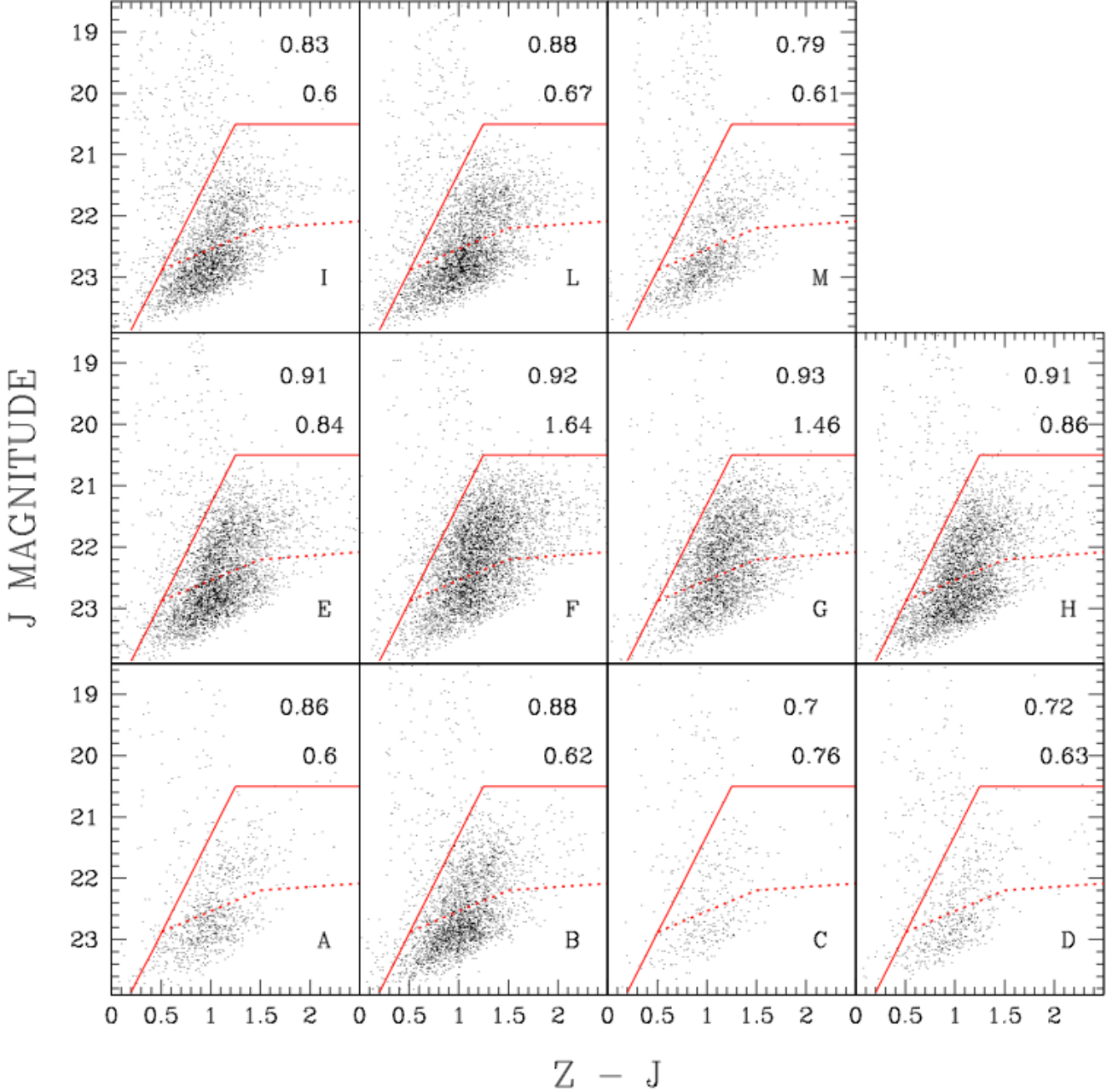


Fig. 19. CMD of catalogue A stars in sub-regions of the tile covering the outer disk of NGC 253, and shown on Fig. 5. The CMDs are identified with the same alphabetic letter as the sub-regions in the outer disk in Fig. 5. The solid line shows the selection criteria for star members of NGC 253; the dotted line shows the location of the tip of the RGB stars as a function of metallicity as in Fig. 6. The two numbers listed in the upper right corner of each panel indicate (uppermost) the fraction of NGC 253 star members over the total number of stars detected in the sub-region (i.e. the same as reported in Fig. 11), and (lowermost) the ratio between the bright AGB stars (counted between the solid and dotted lines) and the RGB stars (counted below the dotted line). The fraction of AGB stars is a function of position in the tile and it increases as we come closer to the disk of NGC 253.

11, Fig. 12, Fig. 20). Counts of sources in catalogue B confirm these findings.

The profile along the whole major axis is plotted on Fig. 13 which illustrates the complementarity of the surface brightness and number counts methods to evaluate the light profile on the disk. Individual star counts become very effective in those regions where the sky subtraction and data reduction systematics become the dominant source of uncertainty for the direct de-

termination of the surface brightness. On the profile we clearly detect a break with a net change of slope, that we interpret as the location of the outer edge of the disk (see also Iodice et al., in prep.). The coordinate at which this break occurs is sensitive to several uncertain factors, among which the most important are the estimate of the sky contribution, and the incompleteness correction applied to the data. As a result, the profile fitting is not well constrained and we place the transition between the disk

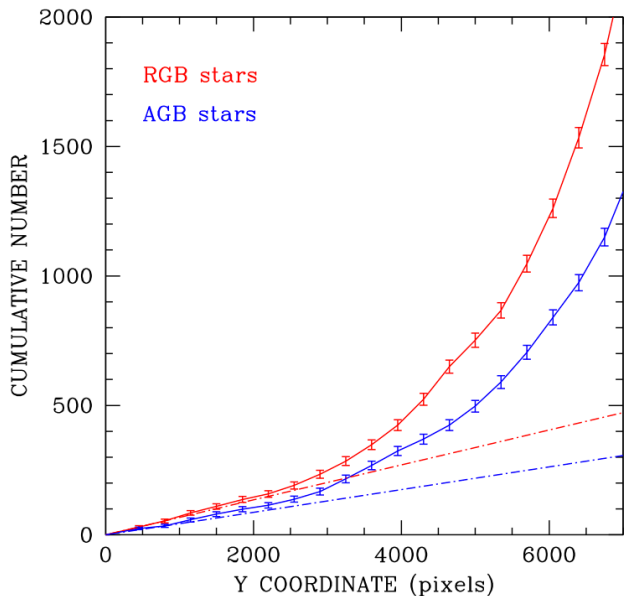


Fig. 20. Solid lines: distribution of the RGB (upper) and AGB (lower) stars extracted from the statistically decontaminated catalogue and located in the central portion of the tile ($2500 \leq X \leq 8500$). The error bars show the $\pm 1\sigma$ Poissonian uncertainty. Dash dotted lines: straight lines fitting the distribution up to $Y = 1000$.

and the inner halo component at a distance between 20 and 25 kpc from the center, the latter value supported by the uncorrected counts in Fig. 12. We remark that the change of slope is detected in the star counts, the surface brightness being affected by a too large uncertainty at such distances from the center. Given the inclination of the NGC 253 galactic plane, we infer then that the thin circular disk is confined to the very central part of the tile (at $7500 \lesssim Y \lesssim 10000$).

The disk appears disturbed, presenting extraplanar components, i.e. the well known *southern shelf* and a substructure in the North which implies an almost symmetric North-South warp in the outer contours of the disk (see Figs. 5, 15, 16). This kind of feature suggests that an event of strong disturbance happened in the past, possibly the merging with a relatively massive galaxy (Davidge 2010). We remark that thanks to the very wide VISTA area surveyed the shape of the disk is very well traced, in particular the northern disturbance is revealed for the first time.

In addition, we detect for the first time a new substructure in the halo of the galaxy, North-West of the main disk. This substructure is evident in the stellar density profiles along the minor axis (Fig. 14) as well as in the contour maps (Figs. 15 and 16). It is located about 28 kpc from the plane of the galaxy along its minor axis, and extends for about 20 kpc. Likely this is a stellar stream remnant of a previous accretion episode. Our photometry only probes the brighter portion of the RGB; this corresponds to a lower limit to the mass of the stellar populations which can be revealed in our counts. From theoretical evolutionary models (Marigo et al. 2008), and assuming a Salpeter-diet IMF as in Section 5, the specific production (i.e. number of stars per unit mass of the parent population) in the upper magnitude bin of the RGB ranges between $\sim (9 \div 3) \times 10^{-5} M_{\odot}^{-1}$ as the age goes from 3 to 10 Gyr, with little dependence on the metallicity. As a consequence, our star counts trace only relatively massive underlying

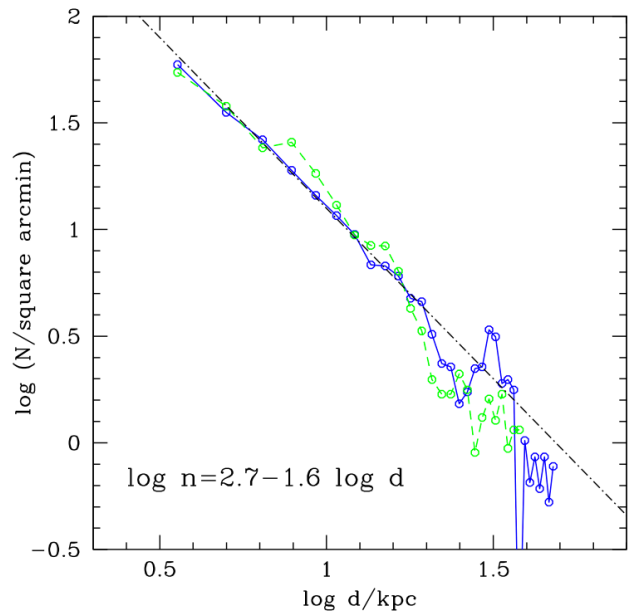


Fig. 21. Surface density profiles of NGC 253 member stars along the minor axis of the disk on a log-log scale. The blue solid line traces the density along the North-West and the green dashed line traces the South East direction. The empirical foreground/background contamination has been subtracted from the counts. The dot-dashed line shows the relation labelled.

populations, i.e. on the average we count 1 bright RGB star per $20000 M_{\odot}$ of parent stellar population. Given our background contamination of 10^4 stars per deg^2 , we estimate a lower limit to the mass surface density of detectable enhancements due to the NGC 253 stellar members of $2 \times 10^8 M_{\odot} / \text{deg}^2$ corresponding to $15 M_{\odot} / \text{arcsecond}^2$, or $0.053 M_{\odot} / \text{pc}^2$ at the distance of NGC 253. A less massive and/or a more disperse stellar population goes undetected below the general background. The substructure mentioned above has a surface density more than twice the background. We estimate the mass of the parent stellar population by determining the excess star counts in the region defined as ($3000 \leq Y \leq 3500$; $1000 \leq X \leq 10000$). In this region we count 780 stars, where, given the area of 0.04 deg^2 , we expect a background of 400 objects. The excess of 380 counts corresponds to a mass of the parent stellar population of $\sim 7.5 \times 10^6 M_{\odot}$. This is an approximate estimate with several factors contributing to its uncertainty. For example, our data suffer from some incompleteness especially at the faint end, so that we could have underestimated the number of bright RGB stars. On the theoretical side, the specific production of bright RGB stars depends on the age and metallicity of the parent stellar population, and our adopted average value could be inaccurate, depending on the actual star formation history of this component. Nevertheless, the above estimate is expected to be correct within a factor of a few (for the assumed IMF), and we speculate that the filamentary structure detected in this region of the halo of NGC 253 is the remnant of an accreted low mass dwarf galaxy, or the nuclear part of a more massive object.

The inner halo appears of elliptical shape close to the disk and tends to become rounder further out, as indicated by the merging of major and minor axis profiles at ~ 35 kpc (Fig. 12), and the excess star counts in Regions 2 and 3 compared

to Regions 1 and 4 in Fig. 11. Our images are not deep enough to allow a robust assessment of the geometry of the halo beyond the outer edge in Fig. 15. Deeper data, yielding a larger number of RGB stars, would have enhanced the statistical significance of the shape of our contours, and lessened the effect of the bright foreground objects.

Fig. 21 shows the profile of the AGB and RGB stars belonging to NGC 253 along the minor axis computed on a central stripe 11.4 kpc wide (the area between the blue long dashed lines in Fig. 15), on a logarithmic scale. The counts in the fiducial region of the CMD have been corrected for the empirical foreground/background contamination of ≈ 1.1 stars per sq.arcmin. The peak at ~ 30 kpc corresponds to the substructure discussed above. On average, the two sides of the profile are extremely similar, and, up to 20 kpc from the galaxy plane, very well represented by a power law with a slope of $n = -1.6$, equivalent to a slope of -4 for the surface brightness profile, when expressed in mag per square arcsec. Beyond 20 kpc the profile seems to become steeper, but the presence of the overdensity at 28 kpc complicates the description of its shape. In addition, we remark that this steepening is much less evident if the counts are not corrected for the foreground/background contamination. Since this correction is uncertain we cannot conclude on the significance of this steepening. The slope of the power law which well describes the inner portion of the halo is not far from what is measured for other spiral galaxies. For M33 Grossi et al. (2011) find $n \approx -2.1$; for M31 Ibata et al. (2007) determines $n = -1.9$, while Tanaka et al. (2010) find $n = -2.2$ and Courteau et al. (2011) an even steeper slope of $n = -2.5$. The reason for the different values obtained fitting the same galaxy is not clear. Theoretical models by Font et al. (2011) predict an average slope of $n = -2.5$ (in the same units) but with large case to case variation. Interestingly, when normalized to the inner region (within 30 kpc), the slope in Font et al. (2011) models is shallower, and values as low as $n = -1.6$ can be found. We conclude that our determined slope is in a broad agreement with the models, although relatively flat.

The panoramic view of the stellar content of the halo of NGC 253 is further illustrated on Fig. 22, showing separately the spatial density map of the foreground plus background contamination, AGB and RGB stars. In the central and right panels, the AGB and RGB averaged counts show the inner structure of the halo and the off-planar perturbation of the disk. The elongation corresponding to the southern shelf and its counterpart in the north side are well visible, especially in the rightmost panel. It is also apparent that the AGB stars are more concentrated in the disk of the galaxy compared to the RGB component, although the different level of incompleteness affecting the two subpopulations is partly responsible for this effect. As already remarked, some AGB stars are found out to large distances from the disk.

A crucial issue is the age of these AGB stars, and in general the star formation history of the whole region sampled by VISTA. We address this question by comparing the observed CMD to theoretical isochrones. Very young stars are absent in the outer disk and halo of NGC 253, and the most recent star formation episodes occurred about 0.3 - 0.5 Gyr ago. The RGB stars are poor age indicators, but in our CMD isochrones as old as 8 Gyr appear well populated. While we cannot assess the age at which star formation began in NGC 253, the CMD is consistent with the presence of stars as old as the oldest stars in the Milky Way. We estimate that the AGB population traces $\sim 2 \times 10^8 M_{\odot}$ of stars formed between 0.5 and 3 Gyr ago, with 75 % of this star formation occurring in the portion of the disk sampled by our CMD. The remaining 25 % is spread out up to large heights above the plane, ≈ 30 kpc or more, as estimated from the profile

of the AGB stars along the minor axis (see Fig. 20). The spatially resolved CMDs constructed for the disk appear quite similar, except for subtle differences which need appropriate simulations to be interpreted with confidence.

The presence of AGB stars over a wide volume as inferred from Fig. 22, is puzzling; either they were accreted, or stripped from/ejected out of the disk, or formed in situ. In the former two cases, the event should have occurred a long time ago, so that the accreted stellar population could mix well in the large volume probed. This seems quite difficult to accomplish within a timescale of 1 Gyr, which is the typical age of the AGB stars. The third possibility, i.e. in situ formation, could find support from the recent detection of a massive molecular wind progressing at high speed from the inner regions of NGC 253 (Bolatto et al. 2013), likely powered by the current starburst. Although this presently ongoing outflow cannot be responsible for the AGB stars in our images, it shows that gas can reach large distances in the galaxy halo. The north-west side of the wind appears to be moving at ~ 400 km/sec. At this velocity the material would reach a 30 kpc distance in 70 Myr. On the other hand, in order to form stars, this gas must slow down and cool, which seems unlikely. In addition, also in this case the smooth distribution of the AGB component requires some substantial time delay from formation to diffusion out of the birth place. Eventually, either option, i.e. accretion or in situ formation, suffer from the same problem, which is the need to mix the AGB population over a wide volume within the stellar lifetime of ~ 1 Gyr. As a possible alternative, this population could be born from a diffuse, very large cloud, but, in the absence of a nearby galaxy, no obvious triggering event is apparent.

7. Conclusions

We present results based on deep *Z* and *J* band VISTA photometry for a field centred on the spiral galaxy NGC 253, that extends up to ~ 40 kpc from the centre along the major axis (in the South-West direction) and up to ~ 50 kpc from the centre along the minor axis (in the North-West direction).

We detect the smooth halo around NGC 253 and one substructure consisting of a ~ 20 kpc wide arc in the north west part of the tile, at about 28 kpc above the plane. Assuming an average metallicity of 0.008 and old age, the excess of 380 counts in this substructure corresponds to a mass of the parent stellar population of $\sim 7.5 \times 10^6 M_{\odot}$.

The star counts suggest that the halo consists of two components, an inner elliptical structure superimposed on a more diffuse possibly spherical halo. Our data are not deep enough to assess the shape of the external halo, but the presence of member stars all over the tile, over more than 50 kpc away from the disk is very well documented.

The wide view of this galaxy confirms the existence of an extra planar region and the disturbed distribution of the outer disk, with the very prominent *southern shelf*, and a symmetrical feature on the north side. This argues for recent interaction for NGC 253, possibly involving an important merging event with another galaxy. However, the stellar population is remarkably homogeneous in the outer disk, and virtually all over the tile. This is surprising. There are strong indication of a recent merger, but no young stars, no young clusters, and no obvious substructures are evident. Particularly puzzling is the distribution of AGB stars. Despite being more centrally concentrated than the RGB stars, 25% of the AGB population is spread all over the halo out to about 30 kpc from the plane. The spatial distribution and ori-

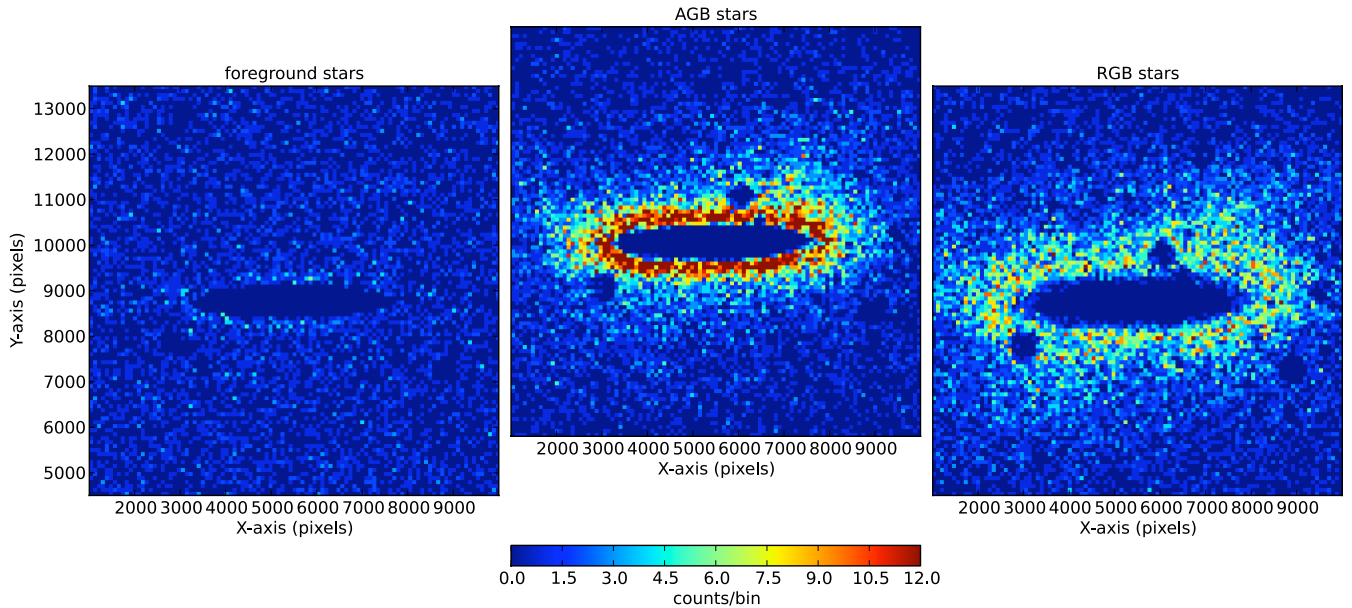


Fig. 22. The stellar density distribution of NGC 253. For each plot, the stellar catalogue has been binned to areas of 0.5×0.5 kpc (87.5×87.5 pixels) and the density of each class of object computed. The foreground population (left panel) shows a very uniform distribution with an average of 0.6 ± 0.8 stars per bin. The AGB stellar density (centre panel) steeply increases toward the disk from background levels to a peak of 27 sources per bin. In contrast, the RGB stars (right panel) are more uniformly distributed around the disk and extend further out. The peak density of the RGB stars is 14 sources per bin.

gin of these stars, whose age should not be older than a few Gyr, deserves further investigation.

Acknowledgements. We thank Jorge Melnick for initiating the VISTA Science Verification and its organization, Thomas Szeifert and Monika Petr-Gotzens for the assistance and help during the observing run, and Jim Lewis, Simon Hodgkin and Eduardo Gonzalez-Solares from CASU for their expert contribution to the VISTA data processing. We also thank Annette Ferguson and Stéphane Courteau for interesting discussions, and the anonymous referee for several useful suggestions that improved the presentation of our results. L.G. thanks ESO for financial support and hospitality to work on this project.

References

- Abadi, M. G., Navarro, J. F., & Steinmetz, M. 2006, *MNRAS*, 365, 747
 Arnaboldi, M., Petr-Gotzens, M., Rejkuba, M., et al. 2010, *The Messenger*, 139, 6
 Arnaboldi, M., Rejkuba, M., Retzlaff, J., et al. 2012, *The Messenger*, 149, 7
 Bailin, J., Bell, E. F., Chappell, S. N., Radburn-Smith, D. J., & de Jong, R. S. 2011, *ApJ*, 736, 24
 Barker, M. K., Ferguson, A. M. N., Irwin, M. J., Arimoto, N., & Jablonka, P. 2012, *MNRAS*, 419, 1489
 Bauer, M., Pietsch, W., Trinchieri, G., et al. 2008, *A&A*, 489, 1029
 Beck, R., Hutschenreiter, G., & Wielebinski, R. 1982, *A&A*, 106, 112
 Bell, E. F., Zucker, D. B., Belokurov, V., et al. 2008, *ApJ*, 680, 295
 Belokurov, V., Zucker, D. B., Evans, N. W., et al. 2006, *ApJ*, 642, L137
 Bolatto, A. D., Warren, S. R., Leroy, A. K., et al. 2013, *Nature*, 499, 450
 Boomsma, R., Oosterloo, T. A., Fraternali, F., van der Hulst, J. M., & Sancisi, R. 2005, *A&A*, 431, 65
 Carollo, D., Beers, T. C., Lee, Y. S., et al. 2007, *Nature*, 450, 1020
 Chonis, T. S., Martínez-Delgado, D., Gabany, R. J., et al. 2011, *AJ*, 142, 166
 Cockcroft, R., McConnachie, A. W., Harris, W. E., et al. 2013, *MNRAS*, 428, 1248
 Comerón, F., Gómez, A. E., & Torra, J. 2003, *A&A*, 400, 137
 Comerón, F., Torra, J., Méndez, R. A., & Gómez, A. E. 2001, *A&A*, 366, 796
 Cooper, A. P., Cole, S., Frenk, C. S., et al. 2010, *MNRAS*, 406, 744
 Courteau, S., Widrow, L. M., McDonald, M., et al. 2011, *ApJ*, 739, 20
 Dalcanton, J. J., Williams, B. F., Seth, A. C., et al. 2009, *ApJS*, 183, 67
 Dalton, G. B., Caldwell, M., Ward, A. K., et al. 2006, in *Society of Photo-Optical Instrumentation Engineers (SPIE) Conference Series*, Vol. 6269, Society of Photo-Optical Instrumentation Engineers (SPIE) Conference Series
 Davidge, T. J. 2010, *ApJ*, 725, 1342
 Emerson, J., McPherson, A., & Sutherland, W. 2006, *The Messenger*, 126, 41
 Engelbracht, C. W., Rieke, M. J., Rieke, G. H., Kelly, D. M., & Achtermann, J. M. 1998, *ApJ*, 505, 639
 Fabbiano, G. & Trinchieri, G. 1984, *ApJ*, 286, 491
 Ferguson, A. M. N., Irwin, M. J., Ibata, R. A., Lewis, G. F., & Tanvir, N. R. 2002, *AJ*, 124, 1452
 Font, A. S., McCarthy, I. G., Crain, R. A., et al. 2011, *MNRAS*, 416, 2802
 Girardi, L., Groenewegen, M. A. T., Hatziminaoglou, E., & da Costa, L. 2005, *A&A*, 436, 895
 Goldsbury, R., Richer, H. B., Anderson, J., et al. 2010, *AJ*, 140, 1830
 Greggio, L., Falomo, R., Zaggia, S., Fantinel, D., & Uslenghi, M. 2012, *PASP*, 124, 653
 Greggio, L. & Renzini, A. 2011, *Stellar Populations. A User Guide from Low to High Redshift* (Wiley-VCH Verlag)
 Grillmair, C. J. 2009, *ApJ*, 693, 1118
 Grossi, M., Hwang, N., Corbelli, E., et al. 2011, *A&A*, 533, A91
 Harris, W. E. 1996, *AJ*, 112, 1487
 Helmi, A. 2004, *MNRAS*, 351, 643
 Helmi, A., Cooper, A. P., White, S. D. M., et al. 2011, *ApJ*, 733, L7
 Hoopes, C. G., Heckman, T. M., Strickland, D. K., et al. 2005, *ApJ*, 619, L99
 Ibata, R., Martin, N. F., Irwin, M., et al. 2007, *ApJ*, 671, 1591
 Ibata, R., Mouhcine, M., & Rejkuba, M. 2009, *MNRAS*, 395, 126
 Ibata, R. A., Gilmore, G., & Irwin, M. J. 1994, *Nature*, 370, 194
 Ibata, R. A., Irwin, M. J., Lewis, G. F., Ferguson, A. M. N., & Tanvir, N. 2003, *MNRAS*, 340, L21
 Ibata, R. A., Lewis, G. F., McConnachie, A. W., et al. 2013, *ArXiv e-prints*
 Irwin, M. J. & Trimble, V. 1984, *AJ*, 89, 83
 Jablonka, P., Tafelmeyer, M., Courbin, F., & Ferguson, A. M. N. 2010, *A&A*, 513, A78
 Jerjen, H., Freeman, K. C., & Binggeli, B. 1998, *AJ*, 116, 2873
 Jurić, M., Ivezić, Ž., Brooks, A., et al. 2008, *ApJ*, 673, 864
 Kaneda, H., Yamagishi, M., Suzuki, T., & Onaka, T. 2009, *ApJ*, 698, L125
 Karachentsev, I. D., Grebel, E. K., Sharina, M. E., et al. 2003, *A&A*, 404, 93
 Lewis, J. R., Irwin, M., & Bunclark, P. 2010, in *Astronomical Society of the Pacific Conference Series*, Vol. 434, *Astronomical Data Analysis Software and Systems XIX*, ed. Y. Mizumoto, K.-I. Morita, & M. Ohishi, 91–+
 Malin, D. & Hadley, B. 1997, *PASA*, 14, 52

- Marigo, P., Girardi, L., Bressan, A., et al. 2008, *A&A*, 482, 883
- Martínez-Delgado, D., Gabany, R. J., Crawford, K., et al. 2010, *AJ*, 140, 962
- Martínez-Delgado, D., Peñarrubia, J., Gabany, R. J., et al. 2008, *ApJ*, 689, 184
- Martínez-Delgado, D., Pohlen, M., Gabany, R. J., et al. 2009, *ApJ*, 692, 955
- McCarthy, I. G., Font, A. S., Crain, R. A., et al. 2012, *MNRAS*, 420, 2245
- McConnachie, A. W., Irwin, M. J., Ibata, R. A., et al. 2009, *Nature*, 461, 66
- Milvang-Jensen, B., Freudling, W., Zabl, J., et al. 2013, *ArXiv e-prints*
- Miskolczi, A., Bomans, D. J., & Dettmar, R.-J. 2011, *A&A*, 536, A66
- Monachesi, A., Bell, E. F., Radburn-Smith, D. J., et al. 2013, *ApJ*, 766, 106
- Mouhcine, M., Ferguson, H. C., Rich, R. M., Brown, T. M., & Smith, T. E. 2005a, *ApJ*, 633, 810
- Mouhcine, M., Ibata, R., & Rejkuba, M. 2010, *ApJ*, 714, L12
- Mouhcine, M., Rich, R. M., Ferguson, H. C., Brown, T. M., & Smith, T. E. 2005b, *ApJ*, 633, 828
- Noel, N. E. D., Greggio, L., Renzini, A., Carollo, M., & Maraston, C. 2013, *ArXiv e-prints*
- Ott, J., Weiss, A., Henkel, C., & Walter, F. 2005, *ApJ*, 629, 767
- Petr-Gotzens, M., Alcalá, J. M., Briceño, C., et al. 2011, *The Messenger*, 145, 29
- Prada, F., Gutierrez, C. M., & McKeith, C. D. 1998, *ApJ*, 495, 765
- Radburn-Smith, D. J., de Jong, R. S., Seth, A. C., et al. 2011, *ApJS*, 195, 18
- Rejkuba, M., Mouhcine, M., & Ibata, R. 2009, *MNRAS*, 396, 1231
- Rieke, G. H., Lebofsky, M. J., Thompson, R. I., Low, F. J., & Tokunaga, A. T. 1980, *ApJ*, 238, 24
- Rieke, G. H., Lebofsky, M. J., & Walker, C. E. 1988, *ApJ*, 325, 679
- Sofue, Y., Wakamatsu, K.-I., & Malin, D. F. 1994, *AJ*, 108, 2102
- Starkenburg, E., Helmi, A., Morrison, H. L., et al. 2009, *ApJ*, 698, 567
- Strickland, D. K., Heckman, T. M., Weaver, K. A., Hoopes, C. G., & Dahlem, M. 2002, *ApJ*, 568, 689
- Tanaka, M., Chiba, M., Komiyama, Y., Guhathakurta, P., & Kalirai, J. S. 2011, *ApJ*, 738, 150
- Tanaka, M., Chiba, M., Komiyama, Y., et al. 2010, *ApJ*, 708, 1168
- Westmoquette, M. S., Smith, L. J., & Gallagher, III, J. S. 2011, *MNRAS*, 414, 3719
- Yanny, B., Newberg, H. J., Grebel, E. K., et al. 2003, *ApJ*, 588, 824
- Zackrisson, E., de Jong, R. S., & Micheva, G. 2012, *MNRAS*, 421, 190
- Zoccali, M., Renzini, A., Ortolani, S., et al. 2003, *A&A*, 399, 931
- Zolotov, A., Willman, B., Brooks, A. M., et al. 2009, *ApJ*, 702, 1058